Thermal conductance and noise of Majorana modes along interfaced $\nu = \frac{5}{2}$ fractional quantum Hall states

Michael Hein [1,2] and Christian Spånslätt [2]

[1]*Department of Physics, University of Konstanz, D-78457 Konstanz, Germany*

[2]*Department of Microtechnology and Nanoscience (MC2), Chalmers University of Technology, S-412 96 Göteborg, Sweden*

Identifying the topological order of the fractional quantum Hall state at filling $\nu = 5/2$ is an important step towards realizing non-Abelian Majorana modes in condensed matter physics. However, to unambiguously distinguish between various proposals for this order is a formidable challenge. Here, we present a detailed study of transport along interfaced edge segments of fractional quantum Hall states hosting non-Abelian Majorana modes. With an incoherent model approach, we compute, for edge segments based on Pfaffian, anti-Pfaffian, and particle-hole-Pfaffian topological orders, thermal conductances, voltage biased charge current noise, and delta-T noise. We determine how the thermal equilibration of edge modes impacts these observables and identify the temperature scalings of transitions between regimes of differently quantized thermal conductances. In combination with recent experimental data, we use our results to estimate thermal and charge equilibration lengths in real devices. We also propose an experimental setup, which permits measuring several transport observables for interfaced fractional quantum Hall edges in a single device. It can, e.g., be used to rule out edge reconstruction effects. In this context, we further point out some subtleties in two-terminal thermal conductance measurements and how to remedy them. Our findings are consistent with recent experimental results pointing towards a particle-hole-Pfaffian topological order at filling $\nu = 5/2$ in GaAs/AlGaAs, and provide further means to pinpoint the edge structure at this filling and possibly also other exotic fractional quantum Hall states.

I. INTRODUCTION

Non-Abelian anyons are exotic excitations in two-dimensional condensed matter systems with no counterpart in particle physics [1]. A system with non-Abelian anyons has a ground-state degeneracy, and interchanging—or braiding—the anyons can shift the system between different ground states. This shift depends only on the order of exchanges and information about the braiding process is stored globally in the ground-state wavefunction. Besides signifying a strongly correlated phase of matter, non-Abelian braiding forms the basis for the appealing, but so far speculative, idea of topologically protected quantum computations [2,3].

A most promising candidate system to host non-Abelian anyons is the fractional quantum Hall (FQH) state [4,5] at filling $\nu = 5/2$ [6–9]. The quantum state that is realized at this filling is, however, still not fully understood and poses a long-standing question in condensed matter physics (see Ref. [10] for a recent overview).

The purpose of this paper is to model FQH edge transport involving various candidate states at this filling, in light of recent experiments [11,12] that have brought progress towards

identifying the 5/2 state. To date, the three most prominent candidate states are the Pfaffian (Pf) [7], anti-Pfaffian (aPf) [13,14], and particle-hole-Pfaffian (phPf) [15–18]. Whereas numerical calculations have seemed to favor the aPf state [19–25], tunneling experiments are more consistent with the aPf, or the Abelian $SU(2)_2$, 331, or 113 states [26–28].

Although all three non-Abelian candidates are (by construction) compatible with the observed Hall conductance $G_H/(e^2/h) = \nu = 5/2$, they have distinct bulk topological orders [29]. Via the bulk-boundary correspondence, this order is in turn manifested by different edge structures, i.e., the number, chirality, and type of channels (or "modes") propagating around the FQH edge. As depicted in Fig. 1, the proposed edge structures of the Pf, aPf, and phPf states differ only in the second Landau level (2LL). This distinction can be quantified by the topological quantum number

$$\nu_Q \equiv c - \bar{c}, \tag{1}$$

where c and $\bar{c}$ are the total central charges for the chiral and antichiral sectors, respectively, in the underlying conformal field theory [30]. For Abelian FQH edges, c ($\bar{c}$) equals the number of "downstream" ("upstream") channels (where the downstream direction is defined as that of the equilibrated charge flow). For more exotic edge structures, c and $\bar{c}$ may take rational values, e.g., $c = 1/2$ for a single non-Abelian Majorana mode (MM). As can be seen in Fig. 1, $\nu_Q^{\text{Pf}} = 7/2$, $\nu_Q^{\text{aPf}} = 3/2$, and $\nu_Q^{\text{phPf}} = 5/2$.
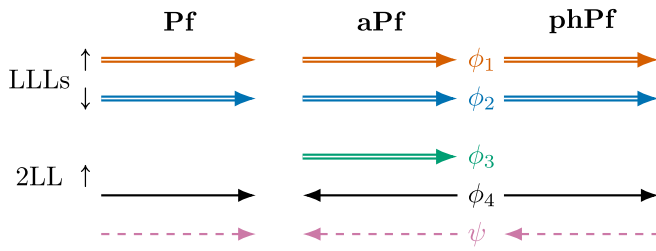
FIG. 1. Edge structures for the Pfaffian (Pf), anti-Pfaffian (aPf), and particle-hole-Pfaffian (phPf) candidate states at filling $\nu = 5/2$. Solid, double arrows (in red, blue, and green) describe integer modes labeled ϕ_1, ϕ_2, and ϕ_3. Black, solid lines describe fractional $1/2$ bosonic modes ϕ_4, and purple, dashed arrows are Majorana modes ψ. The edge modes belong to the two lowest Landau levels (LLLs) or the second (2LL) Landau level. Vertical arrows depict the expected Landau level spin polarizations.

Quite remarkably, the abstract quantity (1) can be related to the experimentally accessible edge thermal conductance G^Q according to the relation [31,32]

$$G^Q = \nu_Q \kappa_0 \bar{T}, \tag{2}$$

in which $\kappa_0 \bar{T} \equiv \pi^2 k_{\mathrm{B}}^2/(3h)\bar{T}$ is the quantum of heat (with k_{B} and h the Boltzmann and Planck constants, respectively, and $\bar{T}$ is the temperature). Two-terminal conductance measurements for QH edges, first demonstrated in Ref. [33], have subsequently been performed for many FQH states in both GaAs/AlGaAs [11,34–37] and graphene [38–41]. In particular, Ref. [35] reported $G^Q/(\kappa_0 \bar{T}) \approx 5/2$ at filling $\nu = 5/2$, which fits well with Eq. (1) for the phPf state (see Fig. 1). This value further rules out Abelian candidate states, since those are incompatible with half-integer G^Q. However, Eq. (2) is valid for the two-terminal conductance only when the heat transport is fully equilibrated, i.e., when edge channels exchange energy efficiently [41–46]. This equilibration can be quantified by a characteristic thermal equilibration length ℓ_{eq}^Q, so that the condition for Eq. (2) to hold reads $\ell_{\mathrm{eq}}^Q \ll L$, where L is the edge length. Importantly, ℓ_{eq}^Q is nonuniversal and depends on microscopic details such as interchannel interactions, the edge disorder strength, and the temperature. It is worth pointing out that an analogous condition, $\ell_{\mathrm{eq}}^C \ll L$, with ℓ_{eq}^C a characteristic charge equilibration length, is needed also for robust charge conductance quantization for FQH edges with counter-propagating modes ($c, \bar{c} \neq 0$). However, almost all FQH experiments to date indicate that this condition is normally well fulfilled (see Refs. [47,48] for exceptions).

The interpretation of the experiment in Ref. [35] as revealing a thermally equilibrated phPf edge was therefore questioned, since $G^Q/(\kappa_0 \bar{T}) \approx 5/2$ can be obtained also for a partially equilibrated aPf edge [49–53]. The same value can, under certain conditions, be obtained from models with random puddles of alternating non-Abelian orders [54–59], or from reentrant states due to Landau level mixing [60].

Further progress has been made recently in GaAs/AlGaAs devices where the $\nu = 5/2$ state is interfaced with integer QH states [11,12]. This results in an effective $\nu = 5/2 - n$ edge, where $n = 1, 2, 3$ (see Fig. 2). The basic idea is that since
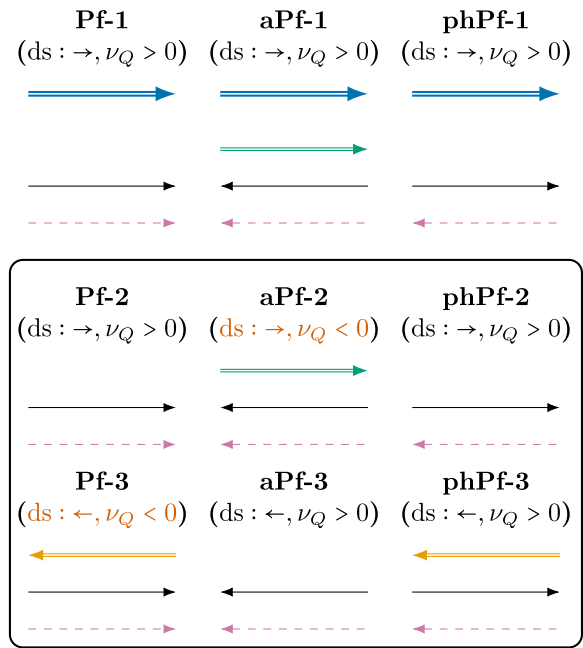

FIG. 2. Effective structures of interfaces between non-Abelian $\nu = 5/2$ candidate states and integer states $n = 1, 2, 3$. In this paper, we focus on $n = 2, 3$ (indicated by the frame), which are the integers that expose the second Landau level. The interfaces with orange text below their name are those for which the directions of equilibrated charge and heat transport are opposite.

all candidate states share two Abelian, integer edge channels (coming from two filled LLLs), successive elimination of them exposes the remaining non-Abelian "$\nu = 1/2$ structure" for which the states differ. This elimination occurs either due to Anderson localization [61–63] or efficient equilibration of the edge states. For $n = 3$, a possible particle-hole symmetry of the 2LL can be tested. In Ref. [11], the thermal conductance for the $\nu = 5/2 - 2$ and $\nu = 5/2 - 3$ edges were both measured to $G^Q/(\kappa_0 \bar{T}) \approx 1/2$. It was argued that this is only possible if the underlying $\nu = 5/2$ state is the phPf, thereby further strengthening the case for this state. It has also been proposed that charge conductance measurements of $5/2 - n$ interfaces could distinguish between non-Abelian candidate states [64].

For the same type of interfaced structures but in another device, the authors in Ref. [12] measured the excess noise for a current biased edge segment. Previously, it was proposed [53,65–67] that such noise discloses important properties of the edge. More specifically, for full thermal and charge equilibration of any edge structure, the noise S scales with L in one of three possible classes: $S \simeq \exp(-L/\ell_{\mathrm{eq}}^C)$ for $\nu_Q > 0$, $S \simeq \sqrt{\ell_{\mathrm{eq}}^C/L}$ for $\nu_Q = 0$, or $S \simeq \mathrm{const.}$ for $\nu_Q < 0$ [66]. This classification holds under conditions where heat leakage into the QH bulk is negligible. If the heat leakage is efficient, the noise is strongly suppressed in L/ℓ_{eq}^C also for $\nu_Q = 0$ and $\nu_Q < 0$. By contrast, under conditions where the thermal equilibration between downstream and upstream modes (if present) is negligible, the noise scales as $S \simeq \mathrm{const.}$, and absence of upstream modes implies identically $S = 0$. This noise classification is the result of the chiral nature of the edge:
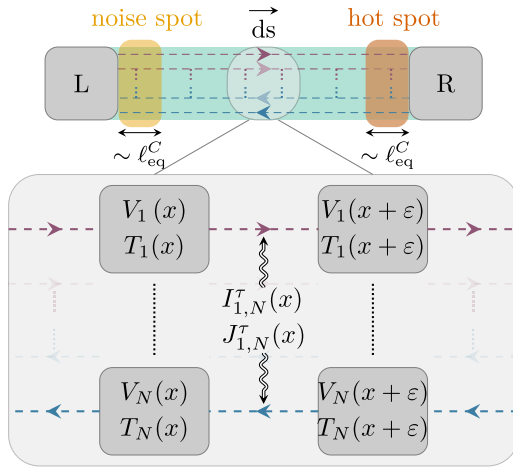
FIG. 3. Schematics of the incoherent edge transport model for a single edge segment with two attached contacts, L and R. A set of N edge channels are characterized by reservoirs with local voltages $V_n(x)$ and temperatures $T_n(x)$ for $n = 1, \ldots, N$. Differences in these quantities drive interchannel charge and energy currents ($I_{n,m}^\tau$ and $J_{n,m}^\tau$ respectively) between the channels, which equilibrate the edge. For equilibrated, chiral charge transport (defining the downstream, ds, direction), Joule heating occurs only in the hot spot (red area) while noise is dominantly produced in the noise spot (yellow area). Equations (3)–(6) are obtained in the continuum limit $N \to \infty$, $\varepsilon \to 0$, with $N/\epsilon = \text{const}$.

For equilibrated charge transport, the voltage drop across a biased edge segment occurs only close to one of the contacts (in the so-called hot spot) whereas partitioning of charges, i.e., excess noise, is dominantly produced close to the other contact (in the so-called noise spot), see Fig. 3. This partitioning is enhanced with respect to the equilibrium noise only in the presence of upstream modes that transport heat from the hot spot to the noise spot. In turn, this heat transport depends strongly on ν_Q, which leads to the correspondence between S and ν_Q.

For an interfaced Pf edge, the classification above implies that only the $5/2 - 3$ interface can generate excess noise, since only that interfacing results in upstream modes. For the aPf, both $5/2 - 1$ and $5/2 - 2$ can result in noise whereas $5/2 - 3$ cannot. Finally, for the phPf, all three interfaces host counter-propagating modes and can therefore produce finite noise. However, since $\nu_Q > 0$ for the phPf interfaces [68], the noise is exponentially suppressed in L/ℓ_{eq}^C and finite noise should only emerge for poor thermal equilibration, i.e., either for small L and/or large ℓ_{eq}^C.

Indeed, Ref. [12] reported finite excess noise for both $5/2 - 2$ and $5/2 - 3$ interfaces for short L, but the noise weakened significantly for larger L (see Fig. 11 below). At the same time, the two-terminal charge conductance of the interface G_{2T} was always measured to $G_{2T}/(e^2/h) = 1/2$, indicating a well-established charge equilibration between downstream and upstream (if present) modes.

TABLE I. Summary of results for the two-terminal thermal conductance G_{2T}^Q, the thermal Hall conductance G_H^Q, as well as charge current noise and delta-T noises for FQH interfaces phPf-n, aPf-n, and Pf-n, where $n \in \{2, 3\}$. Expressions are given in the limits of vanishing, $\alpha, \beta \to 0$, and fully developed, $\alpha, \beta \to \infty$, thermal equilibration. We always assume full charge equilibration: $\delta \gg 1$ and no edge reconstruction. The units of noise are given in terms of voltage bias ΔV or large thermal bias $\Delta T \gg \bar{T}$. The two-terminal charge conductance $G_{2T}/(e^2/h) = 1/2$ for all interfaces.

Interface	Interfaces with three modes: Equilibration parameters α and β $G_{2T}^Q\ [\kappa_0 \bar{T}]$				$G_H^Q\ [\kappa_0 \bar{T}]$
	$\alpha, \beta \to 0$	$\alpha \to \infty$ $\beta \to 0$	$\alpha \to 0$ $\beta \to \infty$	$\alpha, \beta \to \infty$	Universal value
phPf-3	5/2	1/2	3/2	1/2	1/2
aPf-2 and Pf-3	5/2	1/2	3/2	1/2	1/2
	Voltage biased charge current noise $[\Delta V e^3/h]$		Downstream excess delta-T noise $[2G_{2T} k_B \Delta T]$		Upstream excess delta-T noise $[2G_{2T} k_B \Delta T]$	
	$\alpha, \beta \to 0$	$\alpha, \beta \to \infty$	$\alpha, \beta \to 0$	$\alpha, \beta \to \infty$	$\alpha, \beta \to 0$	$\alpha, \beta \to \infty$
phPf-3	$\simeq 0.113$	$\simeq \exp(-\delta)$	$\simeq 0.865$	$\simeq 1$	$\simeq 0.365$	$\simeq \exp(-\delta)$
aPf-2 and Pf-3	$\simeq 0.152$	$\simeq 0.195$	$\simeq 1.361$	$\simeq 1$	$\simeq 0.438$	$\simeq 0.5$

Interface	Interfaces with two modes: Equilibration parameter α $G_{2T}^Q\ [\kappa_0 \bar{T}]$		$G_H^Q\ [\kappa_0 \bar{T}]$
	$\alpha \to 0$	$\alpha \to \infty$	Universal value
phPf-2	3/2	1/2	1/2
aPf-3 and Pf-2	Universal: 3/2		3/2
	Voltage biased charge current noise $[\Delta V e^3/h]$		Downstream excess delta-T noise $[2G_{2T} k_B \Delta T]$		Upstream excess delta-T noise $[2G_{2T} k_B \Delta T]$	
	$\alpha \to 0$	$\alpha \to \infty$	$\alpha \to 0$	$\alpha \to \infty$	$\alpha \to 0$	$\alpha \to \infty$
phPf-2	$\simeq 0.086$	$\simeq \exp(-\delta_{23})$	$\simeq 0.899$	$\simeq 1$	$\simeq 0.338$	$\simeq \exp(-\delta_{23})$
aPf-3 and Pf-2	0	0	1	1	0	0

Taken together, the two experiments [11,12] suggest that the $\nu = 5/2$ state in GaAs/AlGaAs is of phPf type. However, a detailed model of how the upstream mode mediated noise is generated for interfaced $\nu = 5/2$ edges remains lacking. Moreover, the above interpretation of the noise measurements hinges on the absence of edge reconstruction [69–72]. This effect introduces nontopological pairs of counterpropagating modes, which complement the edge structure from the bulk boundary correspondence. The addition of such modes and conditions with poor thermal equilibration can result in noise generation for any FQH edge, which complicates experimental interpretations.

In this paper, we incorporate the qualitative noise and conductance analysis above in a comprehensive theoretical model, which further permits a quantitative comparison with experimental data. To this end, we study transport along interfaces between non-Abelian and integer n edges with the incoherent edge approach, recently developed in Refs. [44,53,65–67,73]. We review the basics of this model in Sec. II. In Secs. III and IV, we use the model to compute the thermal conductance and the noise, respectively, for interfaced edge structures. We focus on $n = 2, 3$, since it is those integers that expose the 2LL structure, see Fig. 2. A summary of the calculations in these sections is given in Table I. In Sec. V, we analyze the temperature scalings of the thermal equilibration lengths. This scaling permits us to analyze the temperature dependence of the noise and thermal conductance. In Sec. VI, we compare our results to the experiments in Refs. [11,12] and provide estimates on thermal and charge equilibration lengths. We then propose in Sec. VII a unified experimental setup allowing several independent experiments for probing FQH edge structures in a single device. We argue that this device is beneficial for ruling out edge reconstruction effects as well as possible sample-to-sample differences between separate devices probing noise and the thermal conductance. We summarize and conclude our paper in Sec. VIII. A number of technical calculations are delegated to Appendixes A–E.

II. MODEL OF EDGE TRANSPORT

A. Charge and energy transport

Our starting point is the generic edge segment with two attached contacts, depicted in Fig. 3. Charge transport along this segment is described by [44,67]

$$\partial_x \vec{V}(x) = \mathcal{M}_V \vec{V}(x). \tag{3}$$

Here, $\vec{V}(x) \equiv [V_1(x), \ldots, V_N(x)]^T$ (with $[\ldots]^T$ denoting vector transpose) describes the local voltages of N edge channels and the matrix

$$\mathcal{M}_V = \begin{pmatrix} -\frac{\sum_{n\neq1}(l_{1,n}^C)^{-1}}{\chi_1 \nu_1} & \frac{(l_{1,2}^C)^{-1}}{\chi_1 \nu_1} & \cdots & \frac{(l_{1,N}^C)^{-1}}{\chi_1 \nu_1} \\ \frac{(l_{2,1}^C)^{-1}}{\chi_2 \nu_2} & -\frac{\sum_{n\neq2}(l_{2,n}^C)^{-1}}{\chi_2 \nu_2} & \cdots & \frac{(l_{2,N}^C)^{-1}}{\chi_2 \nu_2} \\ \vdots & \vdots & \ddots & \vdots \\ \frac{(l_{N,1}^C)^{-1}}{\chi_N \nu_N} & \frac{(l_{N,2}^C)^{-1}}{\chi_N \nu_N} & \cdots & -\frac{\sum_{n\neq N}(l_{N,n}^C)^{-1}}{\chi_N \nu_N} \end{pmatrix} \tag{4}$$

describes couplings between edge channels in terms of the channel chiralities $\chi_i = \pm1$ (with $+1$ and -1 corresponding to downstream and upstream directions, respectively), filling factor discontinuities ν_i, and charge equilibration lengths $l_{i,j}^C = l_{j,i}^C$ between modes i and j. The microscopic content affecting these lengths can be obtained within a chiral Luttinger liquid approach, see e.g., Refs. [39,46,51]. As follows, we always label the modes of all edge structures in Fig. 2 with $i = 1$ starting from the top. The local electric currents $\vec{I}(x) \equiv [I_1(x), \ldots, I_N(x)]^T$, corresponding to $\vec{V}(x)$, obey a similar equation

$$\partial_x \vec{I}(x) = \mathcal{M}_I \vec{I}(x), \quad \mathcal{M}_I = \mathcal{D}_I \mathcal{M}_V \mathcal{D}_I^{-1}, \tag{5}$$

with the diagonal matrix $\mathcal{D}_I = \mathrm{diag}(\chi_1 \nu_1, \ldots, \chi_n \nu_n)$. This description of edge currents was presented also in Ref. [51] and can further be mapped onto the capacitive circuit model in Ref. [74]. Coherence effects between successive interchannel scattering in all these descriptions are neglected (e.g., due to thermal dephasing), which is a prerequisite for robust conductance quantization [42–44,67]. The present model therefore describes incoherent transport along FQH edges, hence the name.

Similarly to the charge transport, edge energy transport is described by

$$\partial_x \vec{T}^2(x) = \mathcal{M}_T \vec{T}^2(x) + \delta\vec{V}(x), \tag{6}$$

where $\vec{T}^2(x) = [T_1^2(x), \ldots, T_N^2(x)]^T$ are the local temperatures (squared), and the matrix

$$\mathcal{M}_T = \begin{pmatrix} -\frac{\sum_{n\neq1}(l_{1,n}^Q)^{-1}}{\chi_1 n_1} & \frac{(l_{1,2}^Q)^{-1}}{\chi_1 n_1} & \cdots & \frac{(l_{1,N}^Q)^{-1}}{\chi_1 n_1} \\ \frac{(l_{2,1}^Q)^{-1}}{\chi_2 n_2} & -\frac{\sum_{n\neq2}(l_{2,n}^Q)^{-1}}{\chi_2 n_2} & \cdots & \frac{(l_{2,N}^Q)^{-1}}{\chi_2 n_2} \\ \vdots & \vdots & \ddots & \vdots \\ \frac{(l_{N,1}^Q)^{-1}}{\chi_N n_N} & \frac{(l_{N,2}^Q)^{-1}}{\chi_N n_N} & \cdots & -\frac{\sum_{n\neq N}(l_{N,n}^Q)^{-1}}{\chi_N n_N} \end{pmatrix} \tag{7}$$

in which $l_{i,j}^Q = l_{j,i}^Q$ are the thermal equilibration lengths (see Appendix A for an example). The final term in Eq. (6) is the Joule heating contribution

$$\delta\vec{V}(x)$$
$$= \frac{e^2}{h\kappa_0} \sum_{n=1}^{N} \left(\frac{[V_1(x) - V_n(x)]^2}{l_{1,n}^C \chi_1}, \ldots, \frac{[V_N(x) - V_n(x)]^2}{l_{N,n}^C \chi_N} \right)^T, \tag{8}$$

and originates from the voltage drops between the edge channels. In the matrix $\mathcal{M}_T$, the thermal conductance of the edge modes are described by the numbers n_i, which equal 1 for Abelian edge channels and 1/2 for Majorana edge channels. These numbers are related to Eq. (1) as

$$c = \sum_{i:\chi_i=+1} n_i, \tag{9}$$

$$\bar{c} = \sum_{i:\chi_i=-1} n_i, \tag{10}$$

$$\nu_Q = \sum_i \chi_i n_i. \tag{11}$$

The local temperatures are further related to local heat currents as

$$J_i(x) = \frac{n_i \kappa_0}{2} T_i^2(x). \tag{12}$$

The transport equations (3) and (6) must be supplemented by boundary conditions that depend on the setup. Boundary conditions are discussed in more detail in Sec. III.

B. Charge current noise

We now focus on the regime of efficient charge equilibration, which we denote as $\delta \equiv L/\ell_{eq}^C \gg 1$, where L is the edge length and

$$\ell_{eq}^C \equiv \max\left(\ell_{i,j}^C\right), \quad \chi_i \times \chi_j = -1, \tag{13}$$

is defined as the largest equilibration length in the set of pairs of counter-propagating channels. As mentioned in Sec. I, this condition is normally fulfilled on all FQH edges. Then, the excess charge current noise S, due to a voltage bias, in any of the two contacts (equal due to charge conservation), see Fig. 3, is to good approximation given by [65,66,75]

$$S \simeq \frac{2e^2}{h\ell_{eq}^C} \frac{v_-}{v_+}(v_+ - v_-) \int_0^L dx\, e^{-\frac{2x}{\ell_{eq}^C}} \Lambda(x). \tag{14}$$

A detailed derivation this formula can be found in Ch. 3 of Ref. [76]. In Eq. (14), "$\simeq$" should here, and below, be understood as "equal in the limit of very large δ". Furthermore,

$$v_+ = \sum_{i:\chi_i=+1} v_i, \tag{15}$$

$$v_- = \sum_{i:\chi_i=-1} v_i, \tag{16}$$

are the total filling factor discontinuities of the downstream ($+$) and upstream ($-$) edge modes respectively. They satisfy the relations $v_+ > v_-$ and $v = v_+ - v_-$, where v is the effective filling factor of the edge structure. For a $5/2 - n$ interface, we simply have $v = 5/2 - n$ for $\delta \gg 1$. The exponential suppression in Eq. (14) follows from the chiral nature of the edge [65]. It implies that the noise generation is predominantly influenced by the region of size $\sim \ell_{eq}^C$ close to the most upstream contact. We call this the noise spot.

The key quantity in Eq. (14) is the local noise kernel

$$\Lambda(x) \equiv \frac{S_{loc}[\delta V(x), T_+(x), T_-(x)]}{2g_{loc}[\delta V(x), T_+(x), T_-(x)]}, \tag{17}$$

where S_{loc} and g_{loc} is the local dc noise and the (dimensionless) tunneling conductance, respectively. It is assumed that all downstream and upstream edge channels charge-equilibrate separately very efficiently, e.g., by emanating from the same (ideal) contact [77]. Importantly, both S_{loc} and g_{loc} depend on microscopic details of the edge such as interchannel interactions, the edge disorder strength, the local voltage difference between the modes $\delta V(x)$, and the thermal equilibration-induced effective temperatures $T_\pm$ of downstream and upstream edge modes. Appendix B outlines how noise kernels are obtained from a bosonization approach.

Our procedure to find the charge and heat flows along an edge segment is as follows. We first solve Eqs. (3) and (6) with
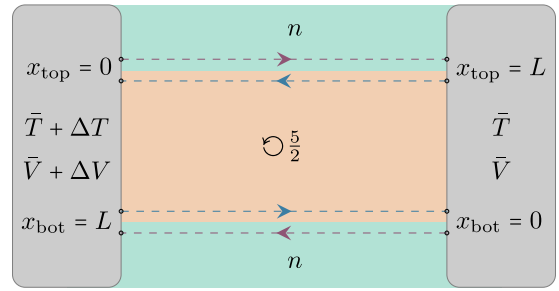

FIG. 4. Schematic two-terminal setup for an interface between regions at filling 5/2 and integers n. For $n < 5/2$, the round arrow depicts the downstream direction (in which the charge current flows) while for $n > 5/2$, it depicts the upstream direction. Swapping the magnetic field direction in the latter case restores the arrow direction to indicate the downstream direction.

suitable boundary conditions. These will depend on the type of setup. We then use these solutions to compute charge and thermal conductances, or insert them first into Eqs. (17) and then (14) to obtain the noise.

III. THERMAL CONDUCTANCE

A. Two-terminal thermal conductance

In this section, we compute the two-terminal thermal conductance for various $5/2 - n$ (with $n = 2, 3$) interfaces by applying Eq. (6) to the setup in Fig. 4. To this end, we set the voltages in both contacts equal to zero, $\bar{V} = \Delta V = 0$. The solutions to Eq. (3) are then trivial, $\bar{V}(x) = 0$. For the thermal transport, the boundary conditions for the top edge segment read

$$T_i(0) = \bar{T} + \Delta T, \quad \text{for} \quad \chi_i = +1, \tag{18a}$$

$$T_i(L) = \bar{T}, \quad \text{for} \quad \chi_i = -1, \tag{18b}$$

and for the bottom segment we have

$$T_i(0) = \bar{T}, \quad \text{for} \quad \chi_i = +1, \tag{19a}$$

$$T_i(L) = \bar{T} + \Delta T, \quad \text{for} \quad \chi_i = -1. \tag{19b}$$

We obtain the heat currents on the top and bottom edge segments by solving Eq. (6) for

$$J_Q^{top} \equiv \sum_{i:\chi_i=+1} J_i(L) - \sum_{i:\chi_i=-1} J_i(L), \tag{20}$$

$$J_Q^{bot} \equiv \sum_{i:\chi_i=+1} J_i(0) - \sum_{i:\chi_i=-1} J_i(0), \tag{21}$$

with $J_i(x)$ given in Eq. (12) [see also Appendix A.9 in Ref. [76] for details in solving Eq. (6)]. Next, by differentiating the total edge current with respect to the temperature difference ΔT, we obtain the two-terminal thermal conductance

$$G_{2T}^Q \equiv \lim_{\Delta T \to 0} \left(\frac{d\left(J_Q^{top} + J_Q^{bot}\right)}{d\Delta T} \right). \tag{22}$$

Let us start with the edge structures Pf-2, and aPf-3, which have only copropagating modes. For both these interfaces, we readily find $G_{2T}^Q/(\kappa_0 \bar{T}) = 3/2$, independently of L and $\ell_{i,j}^Q$, which follows from the fact that the heat exchanged between copropagating channels never backscatters, and such processes can therefore not affect G_{2T}^Q.
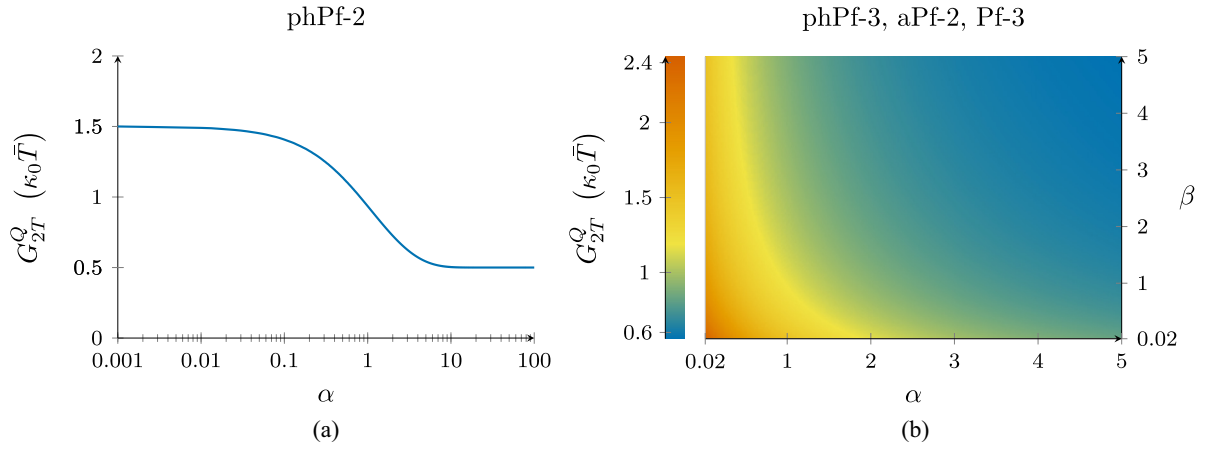
FIG. 5. (a) Two-terminal thermal conductance G_{2T}^Q (in units of the thermal conductance quantum $\kappa_0\bar{T}$) for the phPf-2 interface as a function of the degree of pairwise thermal equilibration α [see Eq. (23)]. (b) G_{2T}^Q as a function of the two equilibration parameters α and β [see Eqs. (23) and (24)] for interfaces phPf-3, aPf-2, and Pf-3.

For the other four interfaces aPf-2, Pf-3, phPf-2, and phPf-3, we consider only pairwise thermal equilibration between the counterpropagating channels, see Fig. 2. Thermal equilibration between co-propagating channels can be ignored, as discussed in the previous paragraph. For example, for the Pf-3 interface, we consider only the thermal equilibration between channel pairs 1-2 and 1-3. As we will show, the thermal conductance then depends on the degrees of thermal equilibration $L/\ell_{i,j}^Q$ between these pairs. To parametrize the equilibration, we introduce two dimensionless equilibration parameters α and β as

$$\alpha = \frac{L}{\ell_{1,2}^Q} \quad \text{and} \quad \beta = \frac{L}{\ell_{1,3}^Q} \quad (23)$$

for the phPf-2, Pf-3, and aPf-2 interfaces and

$$\alpha = \frac{L}{\ell_{1,2}^Q} \quad \text{and} \quad \beta = \frac{L}{\ell_{2,3}^Q} \quad (24)$$

for the phPf-3 structure (note the slight difference in the definition of β, due to their different structures). We plot the thermal conductances as functions of α and β in Fig. 5. For the phPf-2 interface, Fig. 5(a) shows that G_{2T}^Q has a step-like behavior and transitions from $G_{2T}^Q/(\kappa_0\bar{T}) = 1/2 \rightarrow 3/2$ with decreasing α (there is no β parameter for this interface). For large α the thermal transport is effectively mediated by a single, "collective mode" with thermal quantum number $n_{\text{tot}} = 1 - 1/2 = 1/2$. For small α, the two edge channels are essentially decoupled and heat transport occurs in both directions along the edge. The thermal quantum numbers of the channels then add up, $n_{\text{tot}} = 1 + 1/2 = 3/2$, in their contribution to G_{2T}^Q.

The thermal conductance of aPf-2, Pf-3, and phPf-3, is depicted in Fig. 5(b). For these interfaces, we see that, depending on which pair of modes that equilibrates most efficiently, the thermal conductance approaches different limits. More specifically we have

$$\lim_{\substack{\alpha\to\infty \\ \beta\to\infty}} G_{2T}^Q = \tfrac{1}{2}\kappa_0\bar{T}, \quad \lim_{\substack{\alpha\to\infty \\ \beta\to 0}} G_{2T}^Q = \tfrac{1}{2}\kappa_0\bar{T},$$

$$\lim_{\substack{\alpha\to 0 \\ \beta\to\infty}} G_{2T}^Q = \tfrac{3}{2}\kappa_0\bar{T}, \quad \lim_{\substack{\alpha\to 0 \\ \beta\to 0}} G_{2T}^Q = \tfrac{5}{2}\kappa_0\bar{T}. \quad (25)$$

Similar to the phPf-2 interface, the maximum value of the conductance is obtained when there is no thermal equilibration and the contributions of all edge channels along the interface add up, $n_{\text{tot}} = 1 + 1 + 1/2 = 5/2$, as expected. The value $G_{2T}^Q/(\kappa_0\bar{T}) = 1/2$ is generated when all edge channels being fully equilibrated ($\alpha, \beta \to \infty$) and $n_{\text{tot}} = 1 - 1 + 1/2 = 1/2$, in accordance with Eq. (2), up to corrections exponentially small in L. Alternatively, $G_{2T}^Q/(\kappa_0\bar{T}) = 1/2$ is produced for $\alpha \to \infty, \beta \to 0$, where the edge structure becomes a decoupled MM and a pair of two strongly equilibrated bosons, $n_{\text{tot}} = 1/2 + 0$. The zero here corresponds to a diffusive correction, which vanishes as $\sim\alpha^{-1}$ (see, e.g., the Supplemental Material of Ref. [66] for a detailed discussion). In contrast, $G_{2T}^Q/(\kappa_0\bar{T}) = 3/2$ is produced by two decoupled collective modes generating $n_{\text{tot}} = 1/2 + 1 = 3/2$. The limits in Eq. (25) are clearly idealized, and real devices have finite values of α, β. However, to estimate the relative magnitude of α and β requires detailed microscopic information about interchannel energy exchange mechanisms, which generically depend on, e.g., spin, orbital, or valley degrees of freedom of the LLs. Incorporating these effects is a challenging problem, which, however, lies beyond the scope of the present paper.

We end this subsection by pointing out that the experimental value of $G_{2T}^Q/(\kappa_0\bar{T}) = 1/2$ for both $5/2 - 2$ and $5/2 - 3$ can, at least in principle, be generated from a state other than the phPf. Consider an edge structure similar to the aPf edge but with the MM direction reversed. Then, for full thermal equilibration $G_{2T}^Q/(\kappa_0\bar{T}) = 1/2$ is indeed produced for both $n = 2$ and $n = 3$ ($n_{\text{tot}} = 1 - 1 + 1/2 = 1/2$ and $n_{\text{tot}} = 1 - 1/2 = 1/2$, respectively). The nonequilibrated limits for those interfaces are, however, $G_{2T}^Q/(\kappa_0\bar{T}) = 5/2$ and $G_{2T}^Q/(\kappa_0\bar{T}) = 3/2$, respectively, which stand in contrast to the phPf, which has $G_{2T}^Q/(\kappa_0\bar{T}) = 3/2$ and $G_{2T}^Q/(\kappa_0\bar{T}) = 5/2$ in this limit.

B. Thermal Hall conductance

Equation (22) describes the two-terminal thermal conductance, which we have shown to significantly depend on the degree of thermal equilibration. Only for efficient thermal equilibration does G_{2T}^Q take the universal value as specified in Eq. (2). Note that in Eq. (22), the two edge current

contributions are added (cf., Fig. 4). By instead subtracting the two edge currents, one can define a thermal Hall conductance as

$$G_{\mathrm{H}}^{Q} \equiv \lim_{\Delta T \to 0} \left(\frac{d\left(J_{Q}^{\mathrm{top}} - J_{Q}^{\mathrm{bot}}\right)}{d\,\Delta T} \right). \tag{26}$$

In the most general case, the top and bottom edge heat currents depend on all mutual equilibration lengths between all pairs of counterpropagating modes. However, within the model in Sec. II, we prove (see Appendix C for the proof) that for any edge structure, universality emerges

$$G_{\mathrm{H}}^{Q}/(\kappa_0 \bar{T}) = c - \bar{c} = \nu_Q, \tag{27}$$

provided the degrees of *equilibration on the top and bottom edge segments are equal*, even if they are poor. Such a situation can, e.g., be achieved by designing devices with equal top and bottom edge segment lengths. Indeed, such a setup was presented in Ref. [37], in which the thermal Hall conductance was measured at $\nu = 2/3$ and was found to be in good agreement with the expected value $G_{\mathrm{H}}^{Q}/(\kappa_0 \bar{T}) = 0$. At the same time, it was found that $G_{2\mathrm{T}}^{Q}/(\kappa_0 \bar{T}) \approx 0.82$, indicating an incomplete thermal equilibration. In the present context, Figs. 1 and 2 suggest that a Hall type of thermal conductance measurement for interfaces $5/2 - n$ would give $G_{\mathrm{H}}^{Q}/(\kappa_0 \bar{T}) = 7/2 - n$, $3/2 - n$, and $5/2 - n$ for the Pf, aPf, and phPf edges, respectively. A thermal Hall measurement therefore unambiguously distinguishes between these three edge structures. This conclusion holds even in the absence of interfacing, since already $n = 0$ results in different G_{H}^{Q}.

Let us end our treatment of the thermal conductance by emphasizing that for edge states with copropagating channels, there is no significant advantage gained from a thermal Hall measurement. By contrast, for edges with counterpropagating channels, G_{H}^{Q} provides information directly related to the state's topological order, i.e., ν_Q, independent of the thermal equilibration (which might be hard to accurately control experimentally). Finally, we point out that it is simple to check, that within our model, corresponding conclusions hold for a similar definition of the charge Hall conductance as well, i.e.,

$$G_{\mathrm{H}} \equiv \frac{I_{\mathrm{top}} - I_{\mathrm{bot}}}{\Delta V} = \nu \frac{e^2}{h}, \tag{28}$$

when top and bottom charge equilibrations are identical. Here, $I_{\mathrm{top/bottom}}$ are defined in perfect analogy with Eqs. (20) and (21).

IV. NOISE GENERATION ON INTERFACED EDGES

In this section, we compute the noise generated on a single interfaced edge segment with two attached contacts. Such a setup has been realized in experiments, see, e.g., Refs. [12,36,75]. We are here interested in three cases: First, in Sec. IV A, we take the two contacts to have equal temperatures and impose a voltage bias. This is illustrated in Fig 6(a). We then move on to the case with no applied voltage bias, but let the two contacts have different temperatures. Here, we first take the most upstream contact (the left one in the figure) to be the hot one, see Fig 6(b), and compute in Sec. IV B the excess noise in the colder, downstream contact. We call this
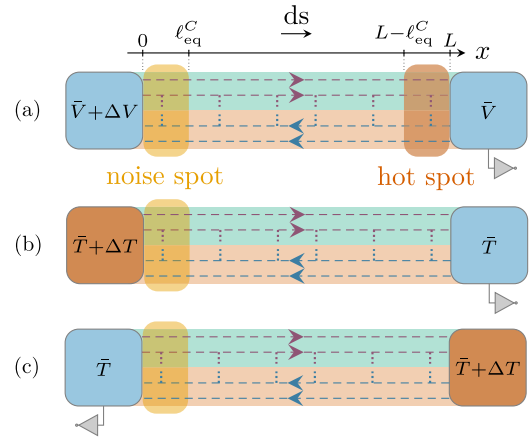

FIG. 6. Schematic setups for measuring charge current noise (in the amplifiers depicted in gray) of a single edge segment in response to (a) a voltage bias, (b) a temperature bias applied in the "downstream" (ds) or (c) "upstream" (us) direction.

downstream delta-T noise. Finally, in Sec. IV C we consider the situation in which the hot contact lies most downstream and the noise is measured in the upstream, colder contact, see Fig 6(c). We call this upstream delta-T noise.

A. Voltage biased edge segment

For an applied voltage bias ΔV, the injected downstream charge current dissipates heat only close to one of the contacts, when the charge equilibration is efficient (the hot spot location is independent of the voltage bias direction [65]). We assume this in the following, which further implies that in the noise spot region, all charged edge modes equilibrate to the same electrochemical potential [65,66]. We can then set $\delta \bar{V}(x \lesssim \ell_{\mathrm{eq}}^{C}) \approx \vec{0}$ [see Eq. (8)], with negligible corrections $\sim \exp[-L/\ell_{\mathrm{eq}}^{C}] \ll 1$ [65]. We further assume that $e\Delta V \gg k_{\mathrm{B}}\bar{T}$, so that in this subsection, we may set the base temperature $\bar{T}$ to zero. Our computed noise then amounts to the excess noise. Such excess noise is generated only if heat from the hot spot can propagate upstream [see Fig. 6(a)]. This possibility depends in turn on the edge structure and on how well the edge channels thermally equilibrate. This feature is captured within our model in Eq. (14). As follows, we consider the two limits of either very efficient or very poor thermal equilibration.

1. Efficient thermal equilibration

For efficient thermal equilibration, we start by solving Eq. (3) for the boundary conditions $V_i(0) = \Delta V$ (we set $\bar{V} = 0$) for $\chi_i = +1$ and $V_i(L) = 0$ for $\chi_i = -1$. This is done for all the charged edge channels. From the solution, we extract the voltage drops (8), which we then insert into Eq. (6), which is finally solved with the boundary conditions $T_i(0) = T_i(L) = 0$. We give examples of voltage and temperature profiles in Appendix D. The resulting temperature profiles are used in Eq. (14). This integral is dominated by the temperatures at the noise spot, i.e., $T_i(x \lesssim \ell_{\mathrm{eq}}^{C})$. Moreover, due to the efficient thermal equilibration, the channel temperatures are similar in this region. Performing the integration in Eq. (14), these two features result in noise on Nyquist-Johnson (NJ)
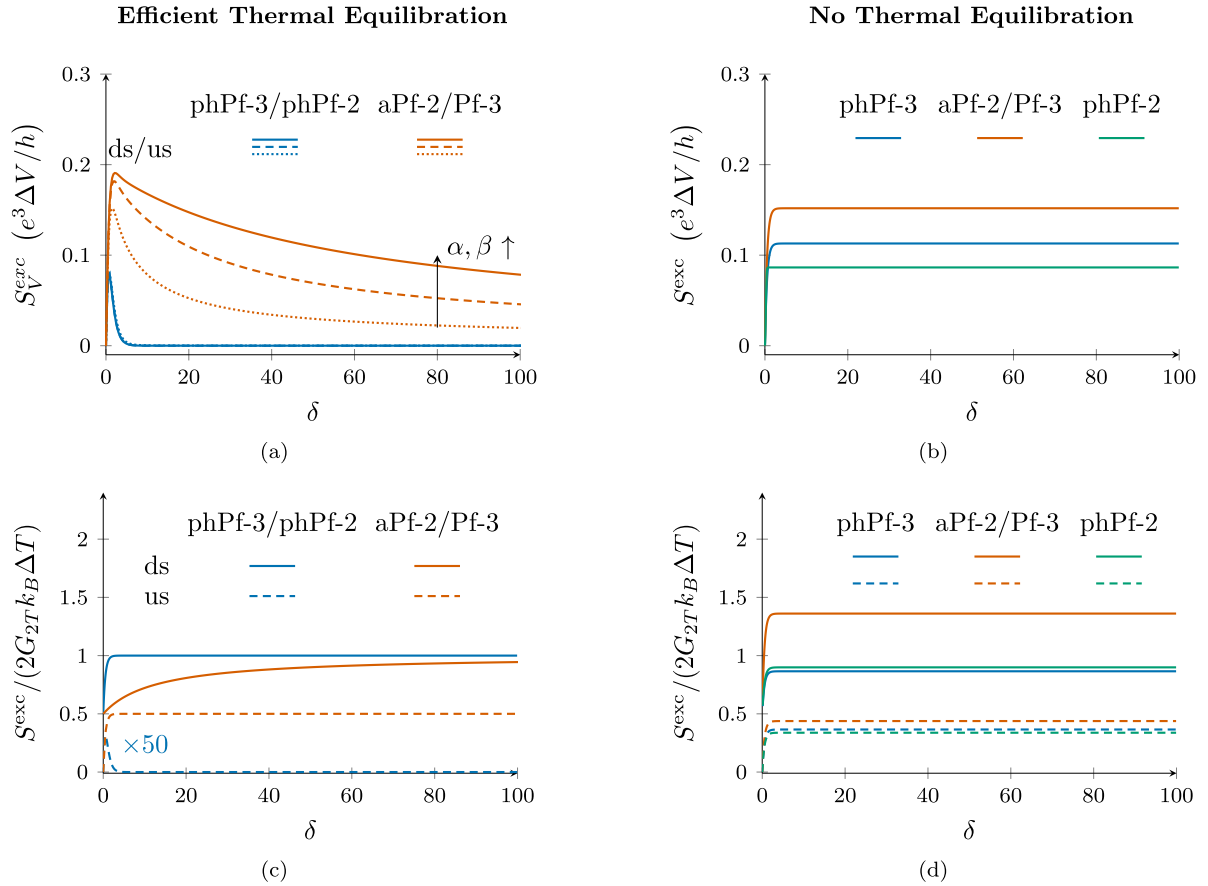
Efficient Thermal Equilibration

No Thermal Equilibration

FIG. 7. (a) Excess (basis temperature $\bar{T} = 0$) noise S^{exc} in units of $e^3 \Delta V / h$, where ΔV is the bias voltage. The noise is computed vs the charge equilibration parameter $\delta = L/\ell_{\text{eq}}^C$ for parameters causing efficient efficient thermal equilibration: $(\alpha, \beta) = \{(250, 250), (100, 100), (25, 25)\}$ [see Eqs. (23) and (24)], for solid, dashed, and dotted lines, respectively. (b) Same as (a) but in the limit of absent thermal equilibration $\alpha, \beta \to 0$. (c) Excess noise in the presence of a temperature gradient ΔT in downstream (ds) or upstream (us) direction for very efficient thermal equilibration with $(\alpha, \beta) = (100, 100)$. (d) Same as (c) but for absent thermal equilibration. For the phPf-2 interface, we have used $\delta = \delta_{23}$, see Fig. 8.

form [78,79]

$$S \simeq \frac{2e^2}{h} \frac{\nu_-}{\nu_+} (\nu_+ - \nu_-) k_B T_{\text{ns}}, \tag{29}$$

in terms of an effective noise spot temperature T_{ns}. This temperature depends on the voltage bias ΔV and the way T_{ns} depends on L stands is in one-to-one correspondence to the three possible cases of a thermally equilbrated edge: $\nu_Q > 0$, $\nu_Q < 0$, and $\nu_Q = 0$ [66]. This classification of the noise was described in detail in Sec. I.

We first analyze the noise generated on the Pf-2 and aPf-3 interfaces. For these, we have that the noise vanishes identically, $S = 0$, for any value of δ and ΔV. This happens simply because there are no upstream modes present that can transport heat to the noise spot, and thus both $\nu_- = 0$ and $\Lambda(x) = 0$ (the latter equality holds because we set $\bar{T} = 0$).

The other four interfaces have $\bar{c} \neq 0$, but the aPf-2 and Pf-3 have $\nu_Q < 0$ whereas phPf-2 and phPf-3 have $\nu_Q > 0$. For these four interfaces, we plot the noise S vs δ in Fig. 7(a). We see that the noise approaches a constant value $S \simeq \text{const.}$ for aPf-2 and Pf-3 but decays exponentially $S \simeq \exp(-\delta)$ for phPf-2 and phPf-3. We also see that with increasing thermal equilibration (increasing α, β) the noise is overall suppressed

for $\nu_Q > 0$, because the heat that reaches the noise spot is suppressed even further. In contrast, when $\nu_Q < 0$, increasing thermal equilibration leads to enhanced noise since, in this case, there is more heat propagating upstream to the noise spot.

2. Absent thermal equilibration

For absent thermal equilibration, downstream and upstream edge modes are generally at very different temperatures at the noise spot. To estimate these temperatures, we follow the approach in Ref. [36] and model the hot spot as a point-like heat source with power [67]

$$P_0 = \frac{e^2 \Delta V^2}{2h} \frac{\nu_-(\nu_+ - \nu_-)}{\nu_+}. \tag{30}$$

We next assume that P_0 is equally divided among all edge channels. The temperature of the modes propagating upstream from the hot spot is thus approximated as

$$T_- \approx \sqrt{\frac{\bar{c}}{c + \bar{c}}} \sqrt{\frac{2P_0}{\kappa_0}}. \tag{31}$$
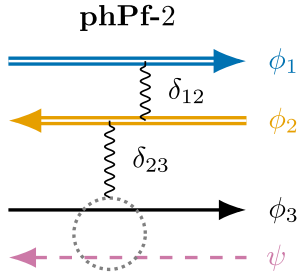
phPf-2

FIG. 8. Edge structure of phPf-2 with an additional pair of counterpropagating integer modes. These modes are responsible for Joule heating in the hot spot and charge partitioning in noise spot.

Since we have set the temperature in the contacts to $\bar{T} = 0$, the downstream modes will have zero temperature at the noise spot

$$T_+ \approx 0. \tag{32}$$

Within the approximations (31) and (32), we compute noise kernels $\Lambda(x)$ in terms of finite and zero-temperature bosonized Green's functions. Details of these calculations are given in Appendix B.

We present the thermally nonequilibrated noise in Fig. 7(b). Similarly to the case of efficient thermal equilibration, the Pf-2, and aPf-3 do not generate any excess noise. For the other interfaces, the noises are essentially constant as functions of δ, since the heat reaching the noise spot is now independent of this parameter. The relative magnitude between the interfaces follow from different noise spot temperatures due to differing prefactors in Eqs. (14) and (31).

The case of the phPf-2 interface warrants here an extra discussion. The noise of this interface was a crucial ingredient in the interpretation of the experiment in Ref. [12]. Figure 1 shows that this structure only has a single downstream charge mode. Hence, no partitioning would be possible and no excess noise could be generated. However, by recalling that on sufficiently small lengthscales, $x \ll \ell_{\text{eq}}^C$, there are in fact counterpropagating integer modes close to both source and drain contacts. These modes are responsible both for Joule heating and charge partitioning. To correctly describe the noise, we include these modes, see Fig. 8. This procedure introduces two charge equilibration lengths between each pair of counterpropagating modes. We parametrize them as $\delta_{12} \equiv L/\ell_{12}^C$ and $\delta_{23} \equiv L/\ell_{23}^C$ in the channel basis $\{\phi_1, \phi_2, \phi_3, \psi\}$ with $\chi = \{+1, -1, +1, -1\}$ and $\nu = \{1, 1, 1/2, 0\}$.

As our next step, we assume that the charge equilibration of the integer channels is much faster than their equilibration with the bosonic 1/2 mode. In terms of our equilibration parameters, this amounts to taking $\delta_{12} \gg \delta_{23}$. The main contribution to the Joule heating then comes from the equilibration of integer channels. This limit is consistent with a quantized expected charge conductance, since we have that

$$\lim_{\substack{\delta_{12} \to \infty \\ \delta_{23} \to 0}} G_{2\text{T}} = \frac{1}{2} \frac{e^2}{h}, \tag{33}$$

which was indeed observed experimentally for the $5/2 - 2$ interface [12]. With this implementation, our model describes how the phPf-2 interface generates noise in the thermally

nonequilibrated limit, see Fig. 7(d). We note that this noise is similar in magnitude as the phPf-3, in accordance with experimental observations [12], see also the discussion in Sec. VI below. We further note that the outlined procedure bares a similarity with implementing edge reconstruction [69–72]. Effects of edge reconstruction are discussed in more detail in Sec. VII.

B. Downstream delta-T noise

Here, we consider the situation where the two contacts are at the same potential, but at different temperatures. Excess charge current noise generated only by a temperature gradient and in the absence of an average charge current, is known as "thermally activated shot noise" or "delta-T noise" [80]. This noise has attracted considerable attention lately (for recent work on delta-T noise for weak tunneling between FQH edges, see Refs. [81–84]). Moreover, delta-T noise is, in fact, at play in two-terminal thermal conductance measurements when the central contact is at zero potential (see Sec. VII below).

We first take the hot contact to lie upstream from the cold contact, see Fig. 6(b). The boundary conditions are then given in Eq. (18). We are interested in the noise in the right, cold contact, which we call downstream delta-T noise (because the noise is measured downstream from the heat source). Note, however, that the noise spot lies close to the hot contact (given that the equilibrated charge flow is from left to right). The noise is given by a modification of Eq. (14), namely,

$$S \simeq \frac{2e^2}{h\ell_{\text{eq}}^C} \frac{\nu_-}{\nu_+}(\nu_+ - \nu_-) \int_0^L dx\, e^{-\frac{2x}{\ell_{\text{eq}}^C}} \Lambda(x)$$
$$+ \frac{2e^2}{h} \frac{(\nu_+ - \nu_-)^2}{\nu_+} k_{\text{B}}(\bar{T} + \Delta T). \tag{34}$$

Here, the second term takes into account thermal fluctuations coming from the hot, left contact [36]. The thermal noise coming from the cold, right contact is suppressed by a factor that is exponential in $\delta = L/\ell_{\text{eq}}^C \gg 1$ [65,76]. This term can thus be safely neglected due to the efficient charge equilibration. In contrast to the voltage biased edge segment (where we assumed $e\Delta V \gg k_{\text{B}}\bar{T} \approx 0$), we focus here on excess noise obtained by subtracting from Eq. (34) the equilibrium noise in the cold contact, i.e.,

$$S^{\text{excess}} \equiv S - 2G_{2\text{T}}k_{\text{B}}\bar{T}, \tag{35}$$

where $G_{2\text{T}} = e^2(\nu_+ - \nu_-)/h$ is the two-terminal charge conductance.

1. Efficient thermal equilibration

For efficient thermal equilibration, we find that the first term in Eq. (34) for any edge structure, reduces to $2e^2\nu_-(\nu_+ - \nu_-)k_{\text{B}}(T + \Delta T)/(h\nu_+)$. Adding this to the second term, we obtain the downstream delta-T noise as

$$S_{\text{ds}} \simeq 2\frac{e^2}{h}(\nu_+ - \nu_-)k_{\text{B}}(\bar{T} + \Delta T)$$
$$= 2G_{2\text{T}}k_{\text{B}}(\bar{T} + \Delta T). \tag{36}$$

λ_{ds}	phPf-3	aPf-2	phPf-2
$\Delta T \ll \bar{T}$	3/4	5/8	4/5
$\Delta T \gg \bar{T}$	0.865	0.774	0.899

TABLE III. Correction factors for thermally nonequilibrated upstream (us) excess delta-T noise [see Eq. (41)] for small and large applied bias ΔT.

λ_{us}	phPf-3	aPf-2	phPf-2
$\Delta T \ll \bar{T}$	3/4	7/8	7/10
$\Delta T \gg \bar{T}$	0.365	0.438	0.338

The corresponding downstream excess noise (35) reduces to

$$S_{\text{ds}}^{\text{excess}} \simeq 2G_{2\text{T}}k_{\text{B}}\Delta T. \tag{37}$$

Hence, the excess downstream delta-T noise for strong thermal equilibration equals the excess NJ-like noise emanating from the hot contact. This result is independent of ν_Q. We also note that for $\Delta T = 0$, the entire edge segment and the contacts are in thermal equilibrium and $S_{\text{ds}} = 2G_{2\text{T}}k_{\text{B}}\bar{T} \Rightarrow S_{\text{ds}}^{\text{excess}} = 0$ as expected. In Fig. 7(c), we plot, for phPf-3, phPf-2, Pf-3, and aPf-2, $S_{\text{ds}}^{\text{excess}}/(2G_{2\text{T}}k_{\text{B}})$ vs δ. We see that with increasing δ this ratio approaches unity as expected. For aPf-3 and Pf-2, where $\bar{c} = 0$, we have trivially $S_{\text{ds}}^{\text{excess}} = 2G_{2\text{T}}k_{\text{B}}\Delta T$ for all δ.

2. Absent thermal equilibration

In case of absent thermal equilibration, edge modes can have very different temperatures at the noise spot. When computing the noise in Eq. (34) for this case, we find that the excess noise still takes a form similar to the NJ noise (37), namely,

$$S_{\text{ds}}^{\text{excess}} = 2\lambda_{\text{ds}}G_{2\text{T}}k_{\text{B}}\Delta T. \tag{38}$$

Here, $\lambda_{\text{ds}} \sim \mathcal{O}(1)$ is a correction factor [36], which reflects the poor thermal equilibration. Its origin is the first term in Eq. (34): For poor thermal equilibration, this term does take the simple form $\sim k_{\text{B}}(T + \Delta T)$ that produced Eq. (36). Instead, we compute (see Appendix B) the noise kernels with distinct temperatures at the noise spot and insert these kernels in Eqs. (34) and (35). We then obtain Eq. (38) with the correction factors λ_{ds}.

In Table II, we give the values of λ_{ds} for weak temperature bias $\Delta T \ll \bar{T}$ and strong bias $\Delta T \gg \bar{T}$ (see Appendix B 2 for the derivation). Note that the values are obtained in the extreme limit of no thermal equilibration, while full equilibration amounts to $\lambda_{\text{ds}} = 1$ according to Eq. (37). Partial equilibration then corresponds to values larger than those in Table II, but still below 1. We use the strong bias values for the plots in Fig. 7(d).

C. Upstream delta-T noise

We now analyze the situation where the hot contact lies downstream to the cold contact, as depicted in Fig. 6(c). The noise is measured in the cold, upstream contact and we call this noise upstream noise (since noise is measured upstream of the heat source). Note that also in this case, the noise spot is close to the left contact. The boundary conditions are now

given in Eq. (19) and the noise reads

$$S \simeq \frac{2e^2}{h\ell_{\text{eq}}^C}\frac{v_-}{v_+}(\nu_+ - \nu_-)\int_0^L dx\, e^{-\frac{2x}{\ell_{\text{eq}}^C}}\Lambda(x)$$
$$+ \frac{2e^2}{h}\frac{(\nu_+ - \nu_-)^2}{\nu_+}k_{\text{B}}\bar{T}. \tag{39}$$

The difference between Eq. (34) and Eq. (39) lies only in the temperature entering the last term: Now the thermal charge fluctuations from the *hot, right contact* are exponentially suppressed in $\delta = L/\ell_{\text{eq}}^C$. The definition of excess noise (35) holds also for the upstream delta-T noise.

1. Efficient thermal equilibration

Whether the noise spot acquires a temperature larger than $\bar{T}$ depends, for efficient thermal equilibration, strongly on the thermal quantum number ν_Q in Eq. (1). For $\nu_Q > 0$, the upstream heat flow is exponentially small in δ and the resulting noise is to excellent approximation given as the NJ noise corresponding to the cold contact

$$S_{\text{us}} \simeq 2G_{2\text{T}}k_{\text{B}}\bar{T}. \tag{40}$$

This implies $S_{\text{us}}^{\text{excess}} = 0$ for all edges with $\nu_Q > 0$. For $\nu_Q \leqslant 0$, the situation is similar to the voltage biased and thermally equilibrated edge in Sec. IV A 1. The only difference is that instead of heat coming from dissipation in the hot spot, it comes from a heated contact. Hence, the classification presented in Ref. [66] (this classification was outlined in Sec. I) carries over to thermally equilibrated, upstream delta-T noise.

We plot the upstream, equilibrated delta-T noise in Fig. 7(c). The interfaces Pf-2, aPf-3, phPf-2, and phPf-3 all have $\nu_Q > 0$ (relative to their charge flows) and their upstream delta-T noises therefore either vanish identically $S = 0$ (aPf-2 and Pf-3) or decay exponentially in δ (aPf-3 and Pf-2). Due to the single Majorana mode on all interfaces, none of them have $\nu_Q = 0$. For aPf-2 and Pf-3, $\nu_Q < 0$ and $S_{\text{us}}^{\text{excess}}$ reaches a constant value with increasing δ.

2. Absent thermal equilibration

For very poor thermal equilibration, upstream excess delta-T noise becomes possible in the presence of upstream modes, $\bar{c} \neq 0$. For $\bar{c} = 0$, we have that $S_{\text{us}} \simeq 2G_{2\text{T}}\bar{T} \Rightarrow S_{\text{us}}^{\text{excess}} \simeq 0$. This is the case for Pf-2 and aPf-3 interfaces.

All other interfaces have $\bar{c} \neq 0$. We compute the noise kernels for those in Appendix B. The resulting noise can be written as

$$S_{\text{us}}^{\text{excess}} = 2\lambda_{\text{us}}G_{2\text{T}}k_{\text{B}}\Delta T, \tag{41}$$

with λ_{us} given in Table III, for both weak, $\Delta T \ll \bar{T}$, and strong temperature bias $\Delta T \gg \bar{T}$. Since the thermally
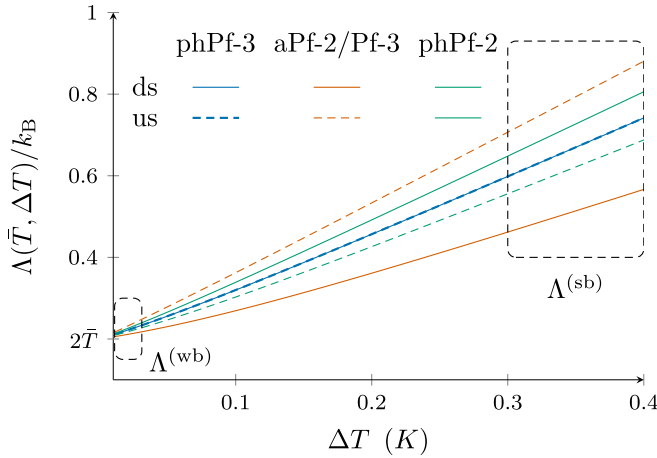
FIG. 9. Noise kernel Λ dependencies on the base temperature $\bar{T}$ (here, we set $\bar{T} = 0.1$ for concreteness) and applied bias ΔT, for poor thermal equilibration. The boxed areas correspond to regions in which the approximation for weak or strong biases (wb and sb, respectively) are valid, see Appendix B 4. The downstream and upstream noise kernels are identical for all ΔT, $\bar{T}$ for the phPf-3 interface.

equilibrated $S_{\mathrm{us}}^{\mathrm{excess}}$ depends on ν_Q, we do not expect a continuous limit for λ_{us}, as was the case for $S_{\mathrm{ds}}^{\mathrm{excess}}$. The strong bias values for λ_{us} are used for the plots in Fig. 7(d): The $\bar{c} \neq 0$ interfaces display constant noise vs δ.

The results for the various types of noise computed in Sec. IV are summarized in Table I.

D. Downstream-upstream symmetry of phPf-3 for absent thermal equilibration

Examination of λ_{ds} and λ_{us} exposes a unique relation for the phPf-3 interface. For strong applied biases, we have for this interface that $\lambda_{\mathrm{ds}} \equiv 0.5 + \lambda_{\mathrm{us}}$. The constant offset follows from Eqs. (34) and (39) together with the fact that for the phPf-3 the noise kernels for excess delta-T noise in the down- and upstream bias configurations are identical, see Appendix B 4. By computing the noise kernels for general $\Delta T / \bar{T}$, we find that the above downstream-upstream symmetry holds for all ΔT (as long as the thermal equilibration is poor). In Fig. 9, this result is visualized by overlapping solid and dashed lines for all ΔT at constant $\bar{T}$ only for the phPf-3 (blue). We present an experimental method to test this symmetry in Sec. VII.

V. TEMPERATURE DEPENDENCE OF THERMAL EQUILIBRATION LENGTHS

Here, we discuss the impact of the base temperature $\bar{T}$ on the thermal equilibration. The degree of this equilibration is determined by parameters on the form L/ℓ_{eq}^Q. Thus, to investigate phenomena related to thermal equilibration, one may either tune L, which requires advanced devices (see, e.g., Ref. [36]), or tune ℓ_{eq}^Q through its temperature dependence. Hence, this dependence is an important edge characteristic, as it determines

(i) The value of the two-terminal thermal conductance G_{2T}^Q for a given temperature $\bar{T}$ and edge length L [41].

(ii) The sharpness of transitions between plateaus of quantized two-terminal thermal conductances (see Sec. III A).

(iii) The magnitude of the noise generated on a single edge segment (see Sec. III B).

In the remainder of this section, we therefore discuss the temperature dependence of various $\ell_{i,j}^Q$ for our considered interfaces.

In Ref. [46], the authors argued that most thermal equilibration lengths scale as

$$\ell_{\mathrm{eq}}^Q \sim \bar{T}^{-2}, \tag{42}$$

due to tunneling of particles between the edge channels. The exponent in (42) comes from the fact that in most cases, the most relevant (in the renormalization group sense) tunneling operators $\mathcal{O}$ take the form

$$\mathcal{O} \sim e^{i \sum_j m_j \phi_j} \text{ or } \sim \psi e^{i \sum_j m_j \phi_j}. \tag{43}$$

Here, ψ is a MM, ϕ_j are bosons, and m_j are real-valued numbers indicating the number and charges of particles that tunnel. When the edge is sufficiently close to a strong disorder fixed point [43,85–87], the m_j take on integer values, which results in an integer scaling dimension of $\mathcal{O}$, denoted Δ [30], and the exponent $\alpha = 2(\Delta - 1)$ in (42) is thus also an integer. Away from such a point, however, the exponents are expected to take on smaller, nonuniversal values, which depend on the interedge interaction strength [43].

An important exception from Eq. (42) is the equilibration length between a counterpropagating boson and Majorana mode. The most relevant operator coupling these modes is instead on the form [46]

$$\mathcal{O} \sim \partial_x \phi \psi i \partial_x \psi. \tag{44}$$

Essentially, Eq. (44) follows from the fact that it is impossible to construct tunneling operators between a counterpropagating boson ϕ and a MM ψ (the point is that only their combination can create electrons), and the simplest operator exchanging energy between the modes is instead of density-density type. This feature leads to the temperature scaling

$$\ell_{\mathrm{eq}}^Q \sim \bar{T}^{-4}. \tag{45}$$

We present a detailed derivation of this result in Appendix A. Equation (45) suggests that, for edges with a counterpropagating boson and a MM, which is the case for phPf-2 and phPf-3 interfaces (see Fig. 2), there can be unusually sharp transitions between thermal conductance plateaus. They are important signatures in thermal conductance measurements. For example, the phPf-3 interface produces a thermal conductance transition from $G_{\mathrm{2T}}^Q/(\kappa_0 \bar{T}) = 1/2$ to $G_{\mathrm{2T}}^Q/(\kappa_0 \bar{T}) = 3/2$ with decreasing temperature $\bar{T}$. The scaling of this transition is of the sharper form (45), which might enhance the prospects of its experimental observation at not too low $\bar{T}$.
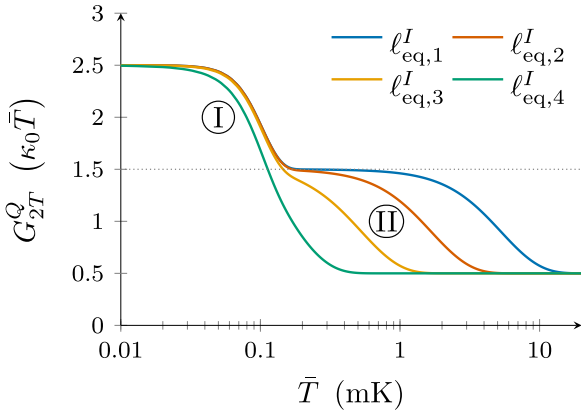
FIG. 10. Two-terminal thermal conductance G_{2T}^Q (in units of the thermal conductance quantum $\kappa_0 \bar{T}$) for $5/2 - 3$ vs $\bar{T}$ for FQH interfaces with three modes and two distinct thermal equilibration lengths. For concreteness, we have chosen numerical values $\ell_{eq,i}^I \sim 5 \cdot \{10^{-5}, 10^{-6}, 10^{-7}, 10^{-8}\} \cdot \bar{T}^{-2}$ and $\ell_{eq}^{II} \sim \{10^{-16}\} \cdot \bar{T}^{-4}$, such that the transitions take place at temperatures below 10 mK.

Temperature scalings of the thermal equilibration lengths enter the incoherent model (summarized in Sec. II), as [39]

$$\ell_{i,j}^Q = \frac{a}{g_{i,j}\gamma_{i,j}(n_i - n_j)} = \frac{a\kappa_0\bar{T}}{G_{i,j}^Q \gamma_{i,j}(n_i - n_j)}, \quad n_i \neq n_j$$

(46a)

$$\ell_{i,j}^Q = \frac{a}{g_{i,j}\gamma_{i,j}} = \frac{a\kappa_0\bar{T}}{G_{i,j}^Q \gamma_{i,j}}, \quad n_i = n_j$$

(46b)

Here, n_i and n_j are the central charges of the two modes, $\gamma_{i,j}$ is a parameter characterizing deviations from the Wiedemann-Franz law [39,44,51], a is the typical lengthscale for interchannel heat exchange, and $G_{i,j}^Q/(\kappa_0\bar{T}) \equiv g_{i,j}$ are the dimensionful and dimensionless thermal conductances of this exchange. The latter quantities can be computed within the chiral Luttinger liquid model (see e.g., Refs. [39,46,51]).

For the special case of the counterpropagating boson and MM, denoted ϕ_2 and ψ, respectively, we have

$$\ell_{\phi,\psi}^Q = \frac{a}{g(n_\phi - n_\psi)\gamma_{\phi,\psi}} = \frac{2a\kappa_0\bar{T}}{G_{int}^Q}$$

(47)

with $\gamma_{\phi,\psi} = 1$ and

$$G_{int}^Q = \frac{8b^2 k_B^4 \pi^5 \Gamma_0^2}{35\hbar^6 v_\phi^2 v_\psi^4} \bar{T}^4 \kappa_0 \bar{T},$$

(48)

as computed in Appendix A. Here, Γ_0 is the bare coupling strength between the channels, which we assume to be weak, and v_ϕ, v_ψ are the propagation velocities of ϕ and ψ, respectively. The parameter b is an ultraviolet cutoff, with dimension of length.

Knowledge of the temperature scalings of $\ell_{i,j}^Q$, permits us to analyze G_{2T}^Q vs $\bar{T}$, rather than α, β (as we did in Sec. III). As an instructive example, we show in Fig. 10 such a plot for the phPf-3 interface. The characteristic feature is the presence of plateaus with different quantized values of G_{2T}^Q. These plateaus are associated to different regimes of equilibrated and nonequilibrated edge modes. In this particular

example, there are two interplateau transitions, which we label *I* and *II*. These transitions are related to thermal equilibration by electron tunneling between ϕ_1 and $\psi \times \phi_2$, transition *I*, and by a density-density interaction between ϕ_2 and the MM ψ, transition *II*. From the above analysis, we have different temperature scalings for these transitions, namely $\ell_{eq}^I \sim \bar{T}^{-2}$ and $\ell_{eq}^{II} \sim \bar{T}^{-4}$. Figure 10 shows that for full thermal equilibration (high $\bar{T}$), $G_{2T}^Q/(k_B\bar{T}) = 1 - 1 + 1/2 = 1/2$, which transitions at lower $\bar{T}$ to the value for absent thermal equilibration, $G_{2T}^Q/(k_B\bar{T}) = 1 + 1 + 1/2 = 5/2$. However, an intermediate plateau emerges in a temperature regime when there is a separation of the two equilibration length scales $\ell_{eq}^I \ll \ell_{eq}^{II}$. This plateau vanishes for $\ell_{eq}^I \approx \ell_{eq}^{II}$ within the range of the transition temperature. A similar analysis can be performed for any edge structure, with its own specific set of plateaus and transitions. The set of these two features can be viewed as a "pin-code" of the FQH edge structure [41].

In the above analysis, we have have neglected interference effects from scattering of bosonic plasmon waves on contact-edge interfaces [43,88,89]. This amounts to assuming $L \gg L_T \sim \bar{T}^{-1}$, where L_T is a characteristic thermal lengthscale. Including the interference effects can potentially generate additional plateaus [36,43].

VI. COMPARISON TO EXPERIMENTS

In this section, we compare the results from our model to the recent experimental findings in Refs. [11,12]. We start with the thermal conductance. In Ref. [11], the two-terminal thermal conductance at the interface between the $5/2$ state and integer states n was observed to obey $G_{2T}^Q/(\kappa_0\bar{T}) \approx |5/2 - n|$. We see that this result is incompatible with both the Pf and aPf edge structures, since for Pf-2 and aPf-3, we have $G_{2T}^Q/(\kappa_0\bar{T}) = 3/2$, independently of the thermal equilibration (see Sec. III A). The measured conductances can further be compared with Fig. 5, where we note that the measured values are consistent with a phPf edge structure, if we assume an efficient thermal equilibration when interfaced with integer modes. Indeed, among the three non-Abelian candidates in Fig. 1, the phPf is the only one compatible with the expected values of G_{2T}^Q for all interfaced structures.

We further note that with decreasing temperature, and thus decreasing degree of equilibration (see Sec. V), the thermal conductance should increase and saturate at $G_{2T}^Q/(\kappa_0\bar{T}) = 3/2$ and $5/2$ for the phPf-2 and phPf-3 edges, respectively. As mentioned in the end of Sec. III A the nonequilibrated limit is an important check for uniquely pinpointing the edge structure. This could be tested in future experiments similar to that in Ref. [41].

We next move on to the noise. Reference [12] reported measurements of excess noise at interfaces of $5/2 - n$ for an applied voltage bias. From our analysis in Sec. III B, we note that for both Pf-2, and aPf-3, which consist of only copropagating modes over long lengthscales, no excess noise is expected for any degree of thermal equilibration. As finite, but with L and $\bar{T}$ decreasing, noise was found for both $5/2 - 2$ and $5/2 - 3$, the most compatible edge structure is, just as in Ref. [12], the phPf, this time assuming the thermal equilibration to be neither full nor absent but rather in an intermediate regime.

Our model allows a comparison on a quantitative level: We compare the measured noise data with our Figs. 7(a) and 7(b). Due to the the well-established charge conductance quantization in Ref. [12], we can safely assume efficient charge equilibration $\delta \gg 1$. From our calculations, we find that the slope of the noise vs bias voltage curve for the phPf-3 interface approximately evaluates to

$$0 \leqslant \partial_{\Delta V} S_{\text{phPf}-3}^{\text{exc}} \leqslant 0.113 \frac{e^3}{h} \approx 0.70 \times 10^{-30} \frac{A^2}{\mu V \, \text{Hz}}, \quad (49)$$

between the two limits of absent and full thermal equilibration (see Appendix E for conversion between units). For this comparison we have chosen $\delta > 10$. The only constraint on δ we have is to reproduce a correctly quantized charge conductance of $G_{2T}/(e^2/h) \approx 1/2$ to good accuracy. Since this is still the case $5 < \delta < 10$, our upper bound for the noise is slightly enhanced for such choices. Access to more accurate estimates of δ from experimental data would improve the accuracy of our noise magnitudes. For the phPf-2 interface, our noise approximately evaluates to

$$0 \leqslant \partial_{\Delta V} S_{\text{phPf}-2}^{\text{exc}} \leqslant 0.086 \frac{e^3}{h} \approx 0.54 \times 10^{-30} \frac{A^2}{\mu V \, \text{Hz}}, \quad (50)$$

i.e., it is of similar magnitude to the one for phPf-3. In comparison, the experimentally observed noise characteristics for both $5/2 - 2$ and $5/2 - 3$ were [12]

$$\partial_{\Delta V} S_{\text{measured}}^{\text{exc}} \approx 0.1 \times 10^{-30} \frac{A^2}{\mu V \, \text{Hz}}, \quad (51)$$

which lies within our estimate and is moreover compatible with interfaced phPf edges that are not fully thermal equilibrated.

We finally estimate the thermal equilibration lengths from noise data measured at lengths $L = \{28, 38, 48, 58\}$ µm in Ref. [12], see Fig. 11. For concreteness, we use the phPf-3 edge structure and compute, for a given set of α, β, δ, the temperature profiles for a given bias $\Delta V \gg \bar{T} \approx 0$. These profiles are then used with Eq. (14) to obtain the noise $S(\alpha, \beta, \delta)$. In Fig. 11, we present $S(L)$ profiles for two sets of model parameters that reasonably reproduce the observed length-dependent noise. For set 1 (blue triangles), we have taken $(\alpha, \beta, \delta) = (6, 10, 100)$ and for set 2 (green triangles), we took $(\alpha, \beta, \delta) = (4, 8, 25)$. For the shortest length $L = 28$ µm, the values $\delta = 100$ and $\delta = 25$ correspond to $\ell_{\text{eq}}^C \approx 0.28$ µm and $\ell_{\text{eq}}^C \approx 1.12$ µm, respectively. Both these charge equilibration lengths accurately produce $G_{2T}/(e^2/h) = 1/2$, as observed experimentally.

For both parameter sets, we find that thermal equilibration lengths

$$3 \, \mu\text{m} \leqslant \left\{\ell_{12}^Q, \ell_{23}^Q\right\} \leqslant 7 \, \mu\text{m} \quad (52)$$

fits the data well.

VII. COMBINED CONDUCTANCE AND NOISE MEASUREMENTS IN A SINGLE DEVICE

In this section, we propose a device designed for measurements of both G_{2T}^Q and various types of noise in a single device, see Fig. 12. This device is beneficial for two main
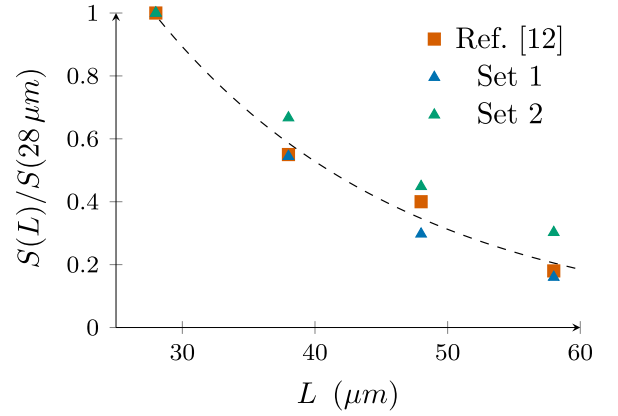

FIG. 11. Length-dependent noise $S(L)$ at the $5/2 - 3$ interface. The red squares and dashed, black line are measured noise data and a fit, respectively, from Ref. [12]. The data is obtained for interface lengths $L = \{28, 38, 48, 58\}$ µm and was normalized to $S(L = 28$ µm$)$. Blue and green triangles is our computed noise for a phPf-3 interface. For the sets 1 and 2, we used parameters $(\alpha, \beta, \delta) = (6, 10, 100)$ and $(\alpha, \beta, \delta) = (4, 8, 25)$ at $L = 28$ µm respectively, to obtain the normalizing constants $S(L = 28 \, \mu\text{m}) = \{0.023, 0.026\}\Delta V \times 10^{-30} A^2/(\mu V \, \text{Hz})$ and thus $S(L)/S(L = 28 \, \mu\text{m})$.
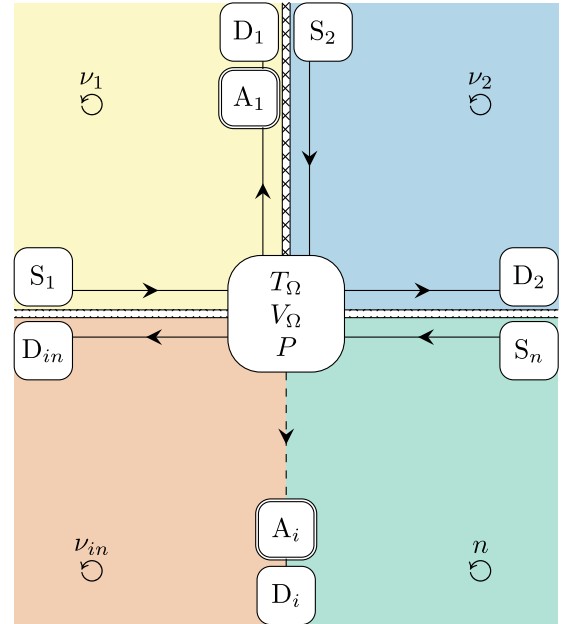

FIG. 12. Schematic setup to measure both the two-terminal thermal conductance and noise for FQH interfaces. The source contacts S_1, S_2, and S_n feed currents into the central contact Ω, dissipating power P and establishing the electrical potential V_Ω, see Eqs. (53) and (54). The dissipated power results in an increased temperature T_Ω, which can be extracted from excess noise in the downstream contact A_1. Heat is carried away from Ω by edge modes along interfaces between gated regions (with fillings ν_1, ν_2, n, and ν_{in}) or with the vacuum (thick, black lines). Upstream noise for the $\nu_{\text{in}} - n$ interface can be measured for either $P = 0, V_\Omega \neq 0$ or $P \neq 0, V_\Omega = 0$, see the text in Sec. VII.

reasons: First, it can be used to rule out possible sample-to-sample differences between separate devices targeted towards noise and conductance measurements. Second, it can be used to exclude effects of edge reconstruction [69–72]. To do so is particularly important, since in its presence, and under conditions of poor thermal equilibration, *any* edge structure can produce excess upstream noise. The benefit with our device is that the two-terminal thermal conductance at poor equilibration gives access to the total number of edge channels (with MM's counted as a "half-channel"). This number can can be used to ascertain that in the noise measurements there is no upstream heat transport in nontopological, spurious upstream modes from edge reconstruction. In describing our device below, we will also point out some subtleties in G_{2T}^Q measurement schemes for states with counter-propagating edge channels, and how to remedy them.

In Fig. 12, four QH regions are connected to a central, floating contact Ω, which can act as a hot reservoir when electrical currents impinge on it. We take the three regions with fillings ν_1, ν_2, and n as the source regions: the source contacts S_1, S_2, and S_n inject currents $I_1 = \nu_1 V_1 e^2/h$, $I_2 = \nu_2 V_2 e^2/h$, and $I_n = nV_n e^2/h$, respectively, and V_1, V_2, and V_n are the corresponding three bias voltages with respect to ground. The drain contacts D_1, D_2, D_i, and D_{in} are grounded, and the amplifiers A_1 and A_i are floating. Note that the currents that emanate from Ω and enter the amplifiers are emitted to grounded contacts. Thus, these currents do not propagate back into source contacts. The filling in the region ν_{in} is here tuned to 5/2 (or to some other state of interest), and this region is interfaced with a region with integer filling n.

The contact potential V_Ω and the dissipated electrical power P can be tuned independently. They are given as

$$V_\Omega = \frac{h}{e^2} \frac{I_1 + I_2 + I_3}{\nu_1 + \nu_2 + \max(\nu_{in}, n)}, \qquad (53)$$

$$P = \frac{h}{2e^2} \left(\frac{I_1^2}{\nu_1} + \frac{I_2^2}{\nu_2} + \frac{I_n^2}{n} - \frac{(I_1 + I_2 + I_n)^2}{\nu_1 + \nu_2 + \max(\nu_{in}, n)} \right). \quad (54)$$

Strictly speaking, Eq. (54) holds when the sourced edges have $\nu_Q > 0$. If this is not the case, it is not evident that all dissipated power heats the central contact. Instead, some Joule heat can leak out back on the source edge via upstream modes, without heating the contact. This produces a correction to Eq. (54), which will influence how the thermal conductance is extracted from the experimental data. We refer to Ref. [36] for a detailed discussion on this issue. However, this possible complication can be avoided by tuning the fillings ν_1 and ν_2 to, e.g., integer values. Then, it is certain that Eq. (54) is the dissipated power in the contact. In the following, we assume that this is the case.

Two operational modes with the device are of particular interest for this paper:

(i) $P = 0$ and $V_\Omega \neq 0$ and the noise in the amplifier A_i is measured vs V_Ω. This configuration realizes the setup in Fig. 6(a), upon the identification $V_\Omega = \Delta V$ and assuming $n < 5/2$. For $n > 5/2$, the charge flow direction along the interface is from A_i to Ω but this flow can be reversed by swapping the magnetic field direction [12]. Since A_i is floating, no net current is injected into Ω for $n > 5/2$. Note that the charge

fluctuations emanating from the hot contact in Fig. 12 is split between four edges. This requires a minor modification of the downstream noise as compared to Secs. IV A and IV B. Specifically, the device geometry is taken into account by substituting in Eqs. (36),(37), (40), and (41),

$$G_{2T} \to G_m^*,$$
$$\frac{1}{G_m^*} = \frac{1}{G_m} + \frac{1}{\sum_{k \neq m} G_k}. \qquad (55)$$

Here, G_m is the equilibrated charge conductance of edge m, where $m = 1$, (in $- n$) labels the two outgoing edges with amplifiers and $k = 1, 2$, in, (in $- n$) labels all outgoing edges.

(ii) $P \neq 0$ and $V_\Omega = 0$. This produces the situations considered in Figs. 6(b) and 6(c). A measurement of the excess noise downstream of the central contact [see Fig. 6(b)] allows to determine its excess temperature $T_\Omega = \bar{T} + \Delta T$. In turn, access to this noise allows extraction of the two-terminal thermal conductance [33]. Let us mention that $V_\Omega = 0$ is not a necessary condition when measuring the thermal conductance. However, finite V_Ω leads to additional hot spots in the device (close to all drain contacts downstream of Ω). In the presence of upstream heat flow, the generated heat at these points could potentially effect the heating of the central contact. Such complications are absent for $V_\Omega = 0$. Ideally, the downstream noise for this purpose is probed on an edge with $\bar{c} = 0$ (e.g., at contact A_1 with ν_1 tuned to an integer). This choice avoids possible corrections to the downstream thermal noise, compare Eq. (36) and Eq. (38). In fact, it is very useful to compare the downstream noises in A_1 and A_i to investigate the validity of the NJ relation [78,79] for QH states with counter-propagating channels and poor thermal equilibration. To illustrate this, we consider ν_1 having only downstream modes. The excess noise in A_1 is then obtained from Eq. (36) as

$$\frac{S_{ds}^{excess,1}}{2G_1^*} = k_B \Delta T. \qquad (56)$$

With the assumption of no upstream modes above, this expression holds independently of any equilibration. In contrast, the excess noise in A_i reads

$$\frac{S_{ds}^{excess,i}}{2G_{in-n}^*} = \lambda_{ds} k_B \Delta T, \qquad (57)$$

where λ_{ds} does depends on the thermal equilibration of the $\nu_{in} - n$ interface. Only for full thermal equilibration is $\lambda_{ds} = 1$.

The ratio between Eq. (56) and Eq. (57) allows extraction of λ_{ds},

$$\lambda_{ds} = \left(\frac{S_{ds}^{excess,i}}{2G_{in-n}^*} \right) \times \left(\frac{S_{ds}^{excess,1}}{2G_1^*} \right)^{-1}. \qquad (58)$$

We next move on to upstream noise measurements. By swapping ν_{in} and n, the noise in A_i corresponds to upstream delta-T noise as presented in Fig. 6(c) [again, the substitution (55) is needed]. Similarly to the downstream delta-T noise, the upstream delta-T can be measured vs ΔT where the latter is obtained from Eq. (56).

Finally, we discuss measurements of the phPf-3 downstream-upstream symmetry of the delta-T noise at poor thermal equilibration, as presented in Sec. IV D. To detect this symmetry, we propose to first measure the downstream delta-T noise (34), but in contrast to the excess noise (35), one subtracts in this case the *hot contact thermal noise*, i.e.,

$$S_{\Delta T}^{\mathrm{ds}} \equiv S - 2G_{\mathrm{in-n}}^{*} k_{\mathrm{B}}(\bar{T} + \Delta T) = \frac{G_{\mathrm{in-n}}^{*}}{2} \Lambda^{\mathrm{ds}}. \quad (59)$$

This quantity can then be compared with the upstream delta-T noise (39) for which the *cold contact thermal noise* is subtracted

$$S_{\Delta T}^{\mathrm{us}} \equiv S - 2G_{\mathrm{in-n}}^{*} k_{\mathrm{B}}\bar{T} = \frac{G_{\mathrm{in-n}}^{*}}{2} \Lambda^{\mathrm{us}}. \quad (60)$$

In going from Eqs. (34) and (39) to Eqs. (59) and (60), we have again used the conductance substitution (55). The downstream-upstream symmetry is now exposed in the ratio

$$\frac{S_{\Delta T}^{\mathrm{ds}}}{S_{\Delta T}^{\mathrm{us}}} = \frac{\Lambda^{\mathrm{ds}}}{\Lambda^{\mathrm{us}}}, \quad (61)$$

which uniquely equals unity for the phPf-3 interface. Comparison of delta-T noises for thermally nonequilibrated interfaces thus provides another experimental signature to distinguish between non-Abelian candidate states.

VIII. SUMMARY AND CONCLUSIONS

We have presented a comprehensive theoretical description of quantum transport along interfaces formed between integer ($n = 2$ and $n = 3$) QH states and non-Abelian Pf, aPf, and phPf candidates for the $\nu = 5/2$ state. Such interfaces isolate the "non-Abelian part" of the edge and was used in recent experiments [11,12], to distinguish between different candidate theories.

For such interfaces and experiments, we have here in detail determined the impact of thermal equilibration on the edge thermal conductance as well as on excess noise on voltage or temperature biased edge segments (so-called delta-T noise). In contrast to Abelian edges, non-Abelian $5/2 - n$ interfaces feature Majorana modes, which although charge neutral, may influence the charge current noise generated on the edge. A major finding is that non-Abelian interfaces with counterpropagating modes are highly sensitive to thermal equilibration. This feature produces a significant length and temperature dependence for the two-terminal thermal conductance. For the noise, the degree of thermal equilibration influences the noise magnitude, the length dependence of the noise, as well as the Nyquist-Johnson relation for charge current noise emanating from a heated contact. Our more quantitative results are summarized in Table I.

In contrast to the two-terminal thermal conductance and the noise, we have proved that for the thermal Hall conductance, as it was defined in Eq. (27), the thermal equilibration dependency drops out for a generic edge structure, *provided the two involved edge segments have the same degree of thermal equilibration*. Such experimental conditions were put forward in Ref. [37]. Our results suggest that a similar experiment performed at $\nu = 5/2$ provides a clear distinction between all candidate states, without any interfacing.

The authors of Refs. [11,12], interpreted their noise and thermal conductance measurements as pointing towards the phPf as the realized state in GaAs/AlGaAs. On the qualitative level, our findings favor such an interpretation as well. We further computed the voltage biased noise for phPf-2 and phPf-3 interfaces, and our results are quantitatively consistent with the experimentally obtained values. Importantly, our calculations show that the measured noise magnitude is indeed consistent with a FQH edge that is not fully thermally equilibrated, which was a crucial feature for the interpretation in Ref. [12].

We would like to further emphasize that the interpretation in Ref. [12] favoring the phPf state is based on the absence of edge reconstruction. If this effect would be present, any edge can generate noise for poor thermal equilibration. This severely complicates the interpretation of the experimental data. Ideally, one would therefore like to confidently rule out such effects. To address this problem, we proposed a device to do precisely that, by allowing thermal conductance and noise measurements in the same sample. Combining such measurements permits an unambiguous determination of the edge structure. We also pointed out some potential issues (highlighted previously in Ref. [36]) with the standard two-terminal thermal conductance setup [33] for edges with counterpropagating modes. Here, we proposed concrete improvements of the setup in order to mitigate these issues.

While our paper targeted the famous $\nu = 5/2$ state, we envision that it can be generalized for the purpose of pinpointing edge structures of other exotic FQH states, such as the even-denominator states in graphene [90–96] or the state at $\nu = 12/5$ [97–99].

Some of the results in this paper were reported in the Master thesis Ref. [76].

APPENDIX A: HEAT EXCHANGE BETWEEN COUNTER-PROPAGATING BOSON AND MAJORANA MODES

The phPf-2 edge structure, depicted in Fig. 2, consists of two modes: One bosonic mode ϕ and one Majorana mode ψ. This structure is valid for lengthscales $L \gg \ell_{\mathrm{eq}}^{C}$, where the contribution of integer edge modes can be neglected. A low-energy effective description of the two counterpropagating modes is then given by the free Lagrangian density

$$\mathcal{L}_0 = \frac{2}{4\pi} \partial_x \phi (\partial_t - v_\phi \partial_x) \partial_x \phi + i\psi(-\partial_t - v_\psi \partial_x)\psi, \quad (A1)$$

where v_ϕ and v_ψ are the mode velocities. Our goal is to compute the heat exchange between the two modes due to a coupling between them. The edge electron operator reads $\psi e^{i2\phi}$, so we cannot introduce electron or quasiparticle tunneling operators to couple these modes. Instead, the simplest, most relevant (in the renormalization group sense) operator coupling the channels is given by the density-density operator [46]

$$\mathcal{O} = \partial_x \phi \psi i \partial_x \psi. \tag{A2}$$

We therefore add to $\mathcal{L}_0$ the point-like perturbation

$$\mathcal{L}_T = \Gamma_0 \delta(x) \partial_x \phi \psi i \partial_x \psi, \tag{A3}$$

where Γ_0 is the coupling constant, assumed to be weak. We thus seek the heat current and intermode thermal conductance induced by $\mathcal{L}_T$, treated as a weak perturbation.

To do so, we consider the unperturbed bosonic energy current, which is given in terms of the stress energy tensor of the upstream bosonic field $\mathcal{T}_\phi \equiv (\partial_x \phi)^2$, as [32]

$$J_{Q,\phi}^{(0)}(d, t) = \hbar \frac{v_\phi^2}{2\pi} \mathcal{T}_\phi(\tilde{t}). \tag{A4}$$

Here, $\tilde{t} = t - \frac{d}{v_\phi}$ is a shifted time referring to the transport of energy a small distance d away from the point $x = 0$. In the interaction picture, the average heat current in the presence of $\mathcal{L}_T$, can be written as

$$\langle J_{Q,\phi}(t) \rangle = \left\langle \mathcal{T} e^{\frac{i}{\hbar} \int_t H'(t)} J_{Q,\phi}^{(0)}(\tilde{t}) e^{-\frac{i}{\hbar} \int_t H'(t)} \right\rangle, \tag{A5}$$

where H' is the Hamiltonian corresponding to $\mathcal{L}_T$, and $\mathcal{T}$ denotes time ordering. We next expand the time-evolution operators up to $\mathcal{O}(\Gamma_0^2)$. Collecting terms corresponding to the same order in Γ_0, the first and second-order correction to the heat current become

$$J_{Q,\phi}^{(1)}(t) = \frac{i}{\hbar} \int_{-\infty}^{t} dt' \left[H'(t'), J_{Q,\phi}^{(0)}(\tilde{t}) \right] \tag{A6}$$

and

$$J_{Q,\phi}^{(2)}(t) = \frac{i^2}{\hbar^2} \int_{-\infty}^{t} dt' \int_{-\infty}^{t'} dt'' \left[H'(t''), \left[H'(t'), J_{Q,\phi}^{(0)}(\tilde{t}) \right] \right], \tag{A7}$$

respectively. The commutators in these expressions can be computed with operator product expansions with the stress energy tensor [30]. After some algebra, we find the corrections to the average energy current in terms of the modes Green's functions as

$$\langle J_{Q,\phi}^{(1)}(t) \rangle = 0 \tag{A8}$$

and

$$\langle J_{Q,\phi}^{(2)}(t) \rangle = \frac{\Gamma_0^2}{\hbar} \int_{-\infty}^{\infty} (\partial_\tau G_\phi(\tau)) \mathcal{G}_\psi(\tau) \, d\tau. \tag{A9}$$

In Eq. (A9), the integrand is given in terms of the finite temperatures Green's functions, $G_\phi(\tau)$ and $\mathcal{G}_\psi(\tau)$ [30], which read

$$G_\phi(\tau) \equiv \langle \partial_x \phi(\tau, 0) \partial_x \phi(0, 0) \rangle$$

$$= \left[\frac{\pi b k_B T_\phi}{\hbar v_\phi} \csc \left(\frac{\pi k_B T_\phi}{\hbar v_\phi} (b - i v_\phi \tau) \right) \right]^2. \tag{A10}$$

with b the UV cutoff, and

$$\mathcal{G}_\psi(\tau) \equiv \langle \mathcal{T}_\psi(\tau, 0) \mathcal{T}_\psi(0, 0) \rangle$$

$$= \left[\frac{\pi b k_B T_\psi}{\hbar v_\psi} \csc \left(\frac{\pi k_B T_\psi}{\hbar v_\psi} (b - i v_\psi \tau) \right) \right]^4$$

$$+ \frac{c^2}{36} \left(\frac{\pi k_B T_\psi}{\hbar v_\psi} \right)^4, \tag{A11}$$

where $c = 1/2$ and $\mathcal{T}_\psi = \psi i \partial_x \psi$ for the MM ψ.

For completeness, we give also the correlation function for a tunneling operator of the form $\mathcal{O} \sim \psi e^{i2\phi_1 + \phi_2}$. From the statistical independence of the involved fields we obtain

$$\langle \mathcal{O}(\tau) \mathcal{O}^\dagger(0) \rangle \propto G_{\phi_1}(\tau) G_{\phi_2}(\tau) G_\psi(\tau), \tag{A12}$$

with

$$G_\phi(\tau) \equiv \langle e^{i v_\phi \phi(\tau, 0)} e^{i v_\phi \phi(0, 0)} \rangle$$

$$= \left[\frac{\pi b k_B T_\phi}{\hbar v_\phi} \csc \left(\frac{\pi k_B T_\phi}{\hbar v_\phi} (b - i v_\phi \tau) \right) \right]^{1/v_\phi} \tag{A13}$$

in which $v_\phi \in \{1/2, 1\}$, and

$$G_\psi(\tau) \equiv \langle \psi(\tau, 0) \psi(0, 0) \rangle$$

$$= \left[\frac{\pi b k_B T_\psi}{\hbar v_\psi} \csc \left(\frac{\pi k_B T_\psi}{\hbar v_\psi} (b - i v_\psi \tau) \right) \right]. \tag{A14}$$

Next, we insert the expressions for $G_\phi(\tau)$ from Eq. (A10) and $\mathcal{G}_\psi(\tau)$ from Eq. (A11) into Eq. (A9) and shift variables $\{\tau \to \tau + i \frac{b}{v_\phi} - i \frac{\hbar \beta_\phi}{2}\}$. Following Ref. [100], the integral boundaries are switched back for a properly introduced cut-off b that satisfies $\hbar v_\phi \beta_\phi > b$. Setting the temperatures $T_\psi = \bar{T} + \frac{\Delta T}{2}$ and $T_\phi = \bar{T} - \frac{\Delta T}{2}$, gives to leading order in ΔT the interaction induced heat current

$$\langle J_{Q,\phi}^{(2)}(t) \rangle = \frac{8 b^2 k_B^6 \pi^7 \Gamma_0^2}{105 \hbar^7 v_\phi^2 v_\psi^4} \bar{T}^5 \Delta T. \tag{A15}$$

The corresponding interaction thermal conductance thus reads

$$G_{\text{int}}^Q = \lim_{\Delta T \to 0} \left(\frac{d}{d \Delta T} \langle J_{Q,\phi}^{(2)} \rangle \right) = \frac{8 b^2 k_B^4 \pi^5 \Gamma_0^2}{35 \hbar^6 v_\phi^2 v_\psi^4} \bar{T}^4 \kappa_0 \bar{T}. \tag{A16}$$

As our final step, we consider an array of points, distanced with the length a, with couplings on the form (A3) and take the continuum limit (see Refs. [39,51,65,67]). This procedure relates the conductance (A16) to the thermal equilibration length as

$$\ell_{\text{eq}}^Q = \frac{a}{g \gamma_{\phi, \psi} (n_\phi - n_\psi)} = \frac{2a}{g \gamma_{\phi, \psi}} = \frac{2a \kappa_0 \bar{T}}{G_{\text{int}}^Q \gamma} \sim \bar{T}^{-4}, \tag{A17}$$

which is Eq. (47). For the interaction (A3), we have $\gamma_{\phi, \psi} = 1$.

APPENDIX B: COMPUTATION OF NOISE KERNELS

Our approach to compute noise kernels $\Lambda(x) = S^{\text{loc}}(x)/[2 g^{\text{loc}}(x)]$ follows that in Ref. [75]. The local noise S^{loc} and local tunneling conductance g^{loc} generically

read

$$S^{\text{loc}}(x) \approx 4 \int_{-\infty}^{\infty} \langle \mathcal{O}(\tau,0) \mathcal{O}^\dagger(0,0) \rangle \, d\tau \tag{B1}$$

and

$$g^{\text{loc}}(x) \approx 2i \int_{-\infty}^{\infty} \tau \langle \mathcal{O}(\tau,0) \mathcal{O}^\dagger(0,0) \rangle \, d\tau. \tag{B2}$$

Here, we have assumed zero-voltage difference between the edge channels, since at the noise spot, edge channels equilibrate to the same electrochemical potential. Furthermore, $\mathcal{O}$ denotes the most relevant tunneling operator coupling charged edge channels, and the corresponding correlation function can be expressed as a product of Green's functions [see Eqs. (A13) and (A14)] as

$$\langle \mathcal{O}(\tau,0) \mathcal{O}^\dagger(0,0) \rangle = \frac{\Gamma_0^2}{(2\pi b)^2} \prod_k G_k(\tau,0). \tag{B3}$$

Here, $k \in \{\psi, \phi_{i \in \{1,2\}}\}$, b is a short distance cut-off, and Γ_0 is the bare coupling amplitude. As follows, we compute $\Lambda(x)$ for various interfaces in the two limiting cases of efficient and absent thermal equilibration. We emphasize that all x dependence in $\Lambda(x)$ enters in the mode temperature profiles $T_k(x)$.

1. Voltage biased charge current noise for absent thermal equilibration

a. phPf-3

For this interface, equilibrated charge transport is from right to left (see Fig. 2). The hot spot and noise spot are therefore interchanged in comparison to Fig. 6(a). Heat from the hot spot is transported upstream by the bosonic 1/2 mode. Absence of thermal equilibration leads, with the procedure outlined in Sec. IV A 2, to the temperatures $T_{\phi_1} = T_\psi = T_+ = 0$ and $T_{\phi_2} = T_- = \sqrt{\frac{4P_0}{5\kappa_0}}$. Following the same approach as in the previous section, using Eqs. (A13) and (A14), we arrive at the noise kernel

$$\Lambda_{\text{phPf}-3}^{\Delta V} = \frac{12\zeta(3)}{\pi^2} k_B T_-, \tag{B4}$$

where $\zeta(z)$ is the Riemann zeta function.

b. aPf-2 and Pf-3

In treating the interfaces aPf-2 and Pf-3, we notice that they are constructed by the same set of modes but in opposite directions. They are therefore expected to generate the same charge current noise and thus to have the same form of $\Lambda(x)$, also in absence of thermal equilibration. With use of Eqs. (31) and (32), the modes' temperatures are given by $T_{\phi_1} = 0$, $T_{\phi_2} \approx T_\psi = T_- = \sqrt{\frac{6P_0}{5\kappa_0}}$, we arrive at

$$\Lambda_{\text{aPf}-2}^{\Delta V} = \Lambda_{\text{Pf}-3}^{\Delta V} \approx 1.604 k_B T_-. \tag{B5}$$

c. phPf-2

For the phPf-2 interface, we take into account an additional pair of integer modes, which are not thermally equilibrated (see the discussion in Sec. IV A 2 and Fig. 8). The charge

transport equation (3) then takes the form

$$\partial_x \vec{V}(x) = \frac{\delta_{12}}{L} \begin{pmatrix} -\chi_1/\nu_1 & \chi_1/\nu_1 & 0 \\ \chi_2/\nu_2 & -\chi_2/\nu_2 & 0 \\ 0 & 0 & 0 \end{pmatrix} \begin{pmatrix} V_1(x) \\ V_2(x) \\ V_3(x) \end{pmatrix}$$
$$+ \frac{\delta_{23}}{L} \begin{pmatrix} 0 & 0 & 0 \\ 0 & -\chi_2/\nu_2 & \chi_2/\nu_2 \\ 0 & \chi_3/\nu_3 & -\chi_3/\nu_3 \end{pmatrix} \begin{pmatrix} V_1(x) \\ V_2(x) \\ V_3(x) \end{pmatrix} \tag{B6}$$

with $\nu_1 = \nu_2 = 1$, $\nu_3 = 1/2$ and $\chi_1 = -\chi_2 = \chi_3 = 1$. The boundary conditions are

$$V_1(0) = \Delta V, \quad V_2(1) = 0 \ , \text{ and } V_3(0) = \Delta V. \tag{B7}$$

To ensure a quantized charge conductance, we choose $\delta_{12} \gg \delta_{23}$. In general it is not possible to give accurate estimates on δ_{12} and δ_{23} without further experimental data. For our purpose it is sufficient to adjust them such that $G_{2T}/(e^2/h) = 1/2$ to good accuracy. Within this description, charge partitioning occurs mainly within the region $0 \lesssim x \lesssim \delta_{12}$. Furthermore, the Joule heating contribution is nonzero and leads to a total dissipated power of

$$P_0 = \frac{3}{\pi^2} \frac{e^2 V_0^2}{h\kappa_0} \int_0^{\delta_{12}} \left[\delta_{12}(V_1 - V_2)^2 + \delta_{23}(V_2 - V_3)^2 \right] dx, \tag{B8}$$

where we omitted the x dependence of V_i for notational ease. The process of interest for the noise characteristics on the phPf-2 edge is the charge tunneling between the bosonic channels of filling $\nu_1 = 1$ and the electronic mode comprised of $\nu_2 = 1/2$ and the MM ψ. Then, the noise kernel for absent thermal equilibration is the same as in the phPf-3 case with the temperature $T_- = \sqrt{\frac{2P_0}{3\kappa_0}}$. Following the same steps as before, the noise is computed vs the charge equilibration length δ_{23}, giving a noise of similar magnitude as for absent thermal equilibration on the phPf-3 edge for a ratio $3 \lesssim \delta_{12}/\delta_{23} \lesssim 5$. The deviation from the expected G_{2T}, is less than 0.5% if $\delta_{23} \gtrsim 8$, which is what we assume here.

2. Downstream delta-T noise for absent thermal equilibration

For this type of noise, the appropriate boundary conditions are given in Eq. (18). We consider the limiting cases of a weak bias (wb), $\Delta T \ll \bar{T}$ and strong bias (sb), $\Delta T \gg \bar{T}$ by expanding the expressions to first order in $\Delta T/\bar{T}$ and setting $\bar{T} = 0$, respectively. We refer to the corresponding noise kernels as $\Lambda^{(\text{wb})}(x)$ and $\Lambda^{(\text{sb})}(x)$, respectively. Following the same steps as in Appendix A, using a shift of variables such that the mode with the largest temperature, say T_m and thus smallest $\beta_m \equiv [k_B(\bar{T} + \Delta T)]^{-1}$ fulfills $\hbar \nu_m \beta_m > b$ and performing the integrals, we arrive at our desired expressions. In case of weak applied bias $\bar{T} \gg \Delta T$, we find to first order in ΔT

$$\Lambda_{\text{phPf}-3}^{(\text{wb})}(x) = 2k_B \bar{T} + k_B \Delta T, \tag{B9a}$$

$$\Lambda_{\text{aPf}-2}^{(\text{wb})}(x) = 2k_B \bar{T} + \frac{k_B}{2} \Delta T, \tag{B9b}$$

$$\Lambda_{\text{phPf}-2}^{(\text{wb})}(x) = 2k_B \bar{T} + \frac{6k_B}{5} \Delta T, \tag{B9c}$$

which reduce to the equilibrium NJ form for vanishing applied bias ΔT as expected. For large bias $\Delta T \gg \bar{T}$ we obtain instead

$$\Lambda_{\text{phPf-3}}^{(\text{sb})}(x) = \frac{12\zeta(3)}{\pi^2} k_B \Delta T, \tag{B10a}$$

$$\Lambda_{\text{aPf-2}}^{(\text{sb})}(x) = \frac{9\zeta(3)}{\pi^2} k_B \Delta T, \tag{B10b}$$

$$\Lambda_{\text{phPf-2}}^{(\text{sb})}(x) = \frac{17\pi^4}{60(\pi^2 \log(4) + 3\zeta(3))} k_B \Delta T. \tag{B10c}$$

3. Upstream delta-T noise for absent thermal equilibration

For the upstream delta-T noise, we use the boundary conditions from Eq. (19). The noise kernels are computed in a similar manner as for the downstream delta-T noise. To first order in ΔT we find for weak applied biases $\Delta T \ll \bar{T}$,

$$\Lambda_{\text{phPf-3}}^{(\text{wb})}(x) = 2k_B \bar{T} + k_B \Delta T, \tag{B11a}$$

$$\Lambda_{\text{aPf-2}}^{(\text{wb})}(x) = 2k_B \bar{T} + \frac{3k_B}{2} \Delta T, \tag{B11b}$$

$$\Lambda_{\text{phPf-2}}^{(\text{wb})}(x) = 2k_B \bar{T} + \frac{4k_B}{5} \Delta T, \tag{B11c}$$

which reduce to equilibrium noise for $\Delta T \to 0$. For strong bias $\Delta T \gg \bar{T}$, we find

$$\Lambda_{\text{phPf-3}}^{(\text{sb})}(x) = \frac{12\zeta(3)}{\pi^2} k_B \Delta T, \tag{B12a}$$

$$\Lambda_{\text{aPf-2}}^{(\text{sb})}(x) = \left(\log(4) + \frac{3\zeta(3)}{\pi^2}\right) k_B \Delta T, \tag{B12b}$$

$$\Lambda_{\text{phPf-2}}^{(\text{sb})}(x) = \frac{\pi^4}{60\zeta(3)} k_B \Delta T. \tag{B12c}$$

4. Downstream-upstream delta-T noise symmetry of phPf-3 at poor thermal equilibration

As depicted in Fig. 9, the most striking feature is that the downstream and upstream noise kernels are uniquely equal for the phPf-3 interface (blue curves in Fig. 9). This equality is clearly manifest also in the asymptotic expressions: compare (B9a) and (B11a), respectively (B10a) and (B12a).

Mathematically, this "downstream-upstream symmetry" follows from the fact that the exponent of the downstream and upstream sectors in the product of edge mode Green's functions [see Eq. (B3)] are equal. More specifically, we have for the phPf-3 interface that

$$G_{\phi_1}(\tau, \bar{T} + \Delta T) G_{\phi_2}(\tau, \bar{T}) G_{\psi}(\tau, \bar{T} + \Delta T)$$
$$\propto G_{\phi_1}(\tau, \bar{T}) G_{\phi_2}(\tau, \bar{T} + \Delta T) G_{\psi}(\tau, \bar{T}). \tag{B13}$$

Here, the first and second line correspond to downstream and upstream bias conditions, respectively. Moreover, the proportionality factor in Eq. (B13), which includes powers of mode velocities and temperatures, crucially drops out when dividing the noise with the conductance to obtain Λ, see Eq. (17). Relations similar to (B13) do not hold for any other edge structure in Fig. 2. Our proposal to test this symmetry is presented in the end of Sec. VII.

5. Some integrals and their computation

In computing the noise kernel for a voltage biased phPf-3 interface, we face integrals

$$S^{\text{loc}} \propto \int_{-\infty}^{\infty} \frac{\text{sech}^2(z)}{(\pi + 2iz)^2} \, dz, \tag{B14}$$

$$g^{\text{loc}} \propto \int_{-\infty}^{\infty} \frac{\text{sech}^2(z)}{\pi + 2iz} \, dz. \tag{B15}$$

Integrals of this kind can be solved by using Mittag-Lefflers' theorem [101], which amounts to expanding the hyperbolic functions as

$$\text{sech}^2(z) = -\sum_{k=0}^{\infty} \left[\frac{1}{(z-A)^2} + \frac{1}{(z+A)^2} \right], \tag{B16}$$

where $A = i\frac{\pi}{2}(2k+1)$. Similar expansions can be found for other hyperbolic functions, e.g., $\text{sech}(z)$. Inserting the series expansion back into Eqs. (B14) and (B15), exchanging the order of integration and summation, we arrive at

$$S^{\text{loc}} \propto \frac{\zeta(3)}{\pi^2} \quad \text{and} \quad g^{\text{loc}} \propto \frac{\pi}{6}. \tag{B17}$$

For other integrals, complex contour integration and the residue theorem are more useful. For example, in the case of delta-T noise at phPf-2 we encounter an integral

$$S^{\text{loc}} \propto \int_{-\infty}^{\infty} \frac{1}{\cosh(z)^3(\pi + 2iz)^2} \, dz. \tag{B18}$$

Substituting $z \to 2\pi t$ and manipulating the resulting expression leads to

$$S^{\text{loc}} \propto \frac{1}{8\pi} \int_{-\infty}^{\infty} \frac{1}{\cosh(2\pi t)^3 \left(\frac{1}{4} - it\right)^2} \, dt. \tag{B19}$$

The right-hand side can now be written as a derivative

$$S^{\text{loc}} \propto -\frac{1}{8\pi} \int_{-\infty}^{\infty} \frac{\partial^2}{\partial a^2} \left(\frac{\ln(a - it)}{\cosh(2\pi t)^3} \right) \Bigg|_{a=1/4} dt$$
$$\equiv -\frac{1}{8\pi} \frac{\partial^2}{\partial a^2} J(a) \Bigg|_{a=1/4}. \tag{B20}$$

We next write the function $J(a)$ as an integral along the closed rectangular contour $\gamma(z)$, defined by

$$-R \to R \to R + i \to -R + i \to -R, \ R \in \mathbb{R}^+, \tag{B21}$$

in the complex z plane as

$$J(a) = -\oint_{\gamma(z)} \frac{\ln(\Gamma(a - iz))}{\cosh(2\pi z)^3} dz$$
$$= -2\pi i \sum_i \text{Res}\left(\frac{\ln(\Gamma(a - iz))}{\cosh(2\pi z)^3}, z_i \right), \tag{B22}$$

where we used the residue theorem in the final step with the two third-order poles $z_1 = i/4$ and $z_2 = 3i/4$ enclosed by $\gamma(z)$. After some additional algebraic manipulations, we arrive at

$$J(a) = \frac{1}{8\pi^2} \left[\psi^{(1)}(a + 3/4) - \psi^{(1)}(a + 1/4) \right]$$
$$+ \frac{1}{2} \left[\ln(\Gamma(a + 3/4)) - \ln(\Gamma(a + 1/4)) \right], \tag{B23}$$

where $\psi^{(1)}(z) = \partial_z^2 \ln \Gamma[z]$ is the trigamma function. Combining Eqs. (B20) and (B23) gives

$$\frac{1}{8\pi} \int_{-\infty}^{\infty} \frac{1}{\cosh(2\pi t)^3 \left(\frac{1}{4} - it\right)^2} \, dt = \frac{17\pi}{480}. \tag{B24}$$

The same method be can be used to produce the following identity:

$$\int_{-\infty}^{\infty} \frac{1}{\cosh(2\pi t)^3 (a - it)^n} \, dt = \frac{(-1)^{n-1}}{(n-1)!} \frac{d^n J(a)}{da^n}, \ n \in \mathbb{Z}^+. \tag{B25}$$

APPENDIX C: PROOF OF THE UNIVERSALITY OF G_H^Q FOR EQUAL THERMAL EQUILIBRATION ON TOP AND BOTTOM EDGES

Here, we prove Eq. (27), namely that the thermal Hall conductance (26) is universal as long as the two edges have the same degree of equilibration (even if it is poor).

We consider a generic edge structure with k downstream (ds) and $N - k$ upstream (us) modes, and write the heat transport equation (6) (with $\delta \vec{V} = 0$, since we assume no voltage bias) as

$$\partial_x \vec{\theta}(x) = \mathcal{M}_T \vec{\theta}(x). \tag{C1}$$

Here, we defined $\vec{\theta}(x) = \vec{T}^2(x)$, and the matrix $\mathcal{M}_T$ (7) satisfies the heat current conservation law

$$\sum_j (\mathcal{M}_T)_{ij} = 0, \quad \forall i. \tag{C2}$$

The general solution of Eq. (C1) for an edge segment with length $L > 0$ can be written as

$$\vec{\theta}(L) = e^{L\mathcal{M}_T} \vec{\theta}(0), \tag{C3}$$

which we express in ds and us blockform as

$$\begin{pmatrix} \vec{\theta}_{ds}(L) \\ \vec{\theta}_{us}(L) \end{pmatrix} = \begin{pmatrix} \mathcal{A} & \mathcal{B} \\ \hline \mathcal{C} & \mathcal{D} \end{pmatrix} \begin{pmatrix} \vec{\theta}_{ds}(0) \\ \vec{\theta}_{us}(0) \end{pmatrix}. \tag{C4}$$

Here, the block matrices $\mathcal{A} \in \mathbb{R}^{k \times k}$, $\mathcal{B} \in \mathbb{R}^{k \times (N-k)}$, $\mathcal{C} \in \mathbb{R}^{(N-k) \times k}$, and $\mathcal{D} \in \mathbb{R}^{(N-k) \times (N-k)}$. In terms of these matrices, the heat conservation law (C2) translates to

$$\sum_j \mathcal{A}_{ij} + \sum_j \mathcal{B}_{ij} = 1, \quad \forall i, \tag{C5}$$

$$\sum_j \mathcal{C}_{ij} + \sum_j \mathcal{D}_{ij} = 1, \quad \forall i. \tag{C6}$$

Next, we rearrange the terms in Eq. (C4) as

$$\begin{pmatrix} \vec{\theta}_{ds}(L) \\ \vec{\theta}_{us}(0) \end{pmatrix} = \begin{pmatrix} \mathcal{A} - \mathcal{B}\mathcal{D}^{-1}\mathcal{C} & \mathcal{B}\mathcal{D}^{-1} \\ \hline -\mathcal{D}^{-1}\mathcal{C} & \mathcal{D}^{-1} \end{pmatrix} \begin{pmatrix} \vec{\theta}_{ds}(0) \\ \vec{\theta}_{us}(L) \end{pmatrix}. \tag{C7}$$

Let us now consider the top edge, for which the boundary conditions read $\vec{\theta}_{ds}(0) = (\bar{T} + \Delta T)^2 \times (1, \ldots, 1)_k^T$ and $\vec{\theta}_{us}(L) = \bar{T}^2 \times (1, \ldots, 1)_{N-k}^T$ (see Fig. 4). Plugging these quantities into

Eq. (C7), we write the top edge heat current (20) as

$$J_Q^{top} = \frac{\kappa_0}{2} \left(\sum_{i:\chi_i=+1} n_i \theta_{ds}^i(L) - \bar{T}^2 \sum_{i:\chi_i=-1} n_i \right)$$

$$= \frac{\kappa_0}{2} \left((\bar{T} + \Delta T)^2 \sum_{i,j:\chi_i=+1} n_i (\mathcal{A} - \mathcal{B}\mathcal{D}^{-1}\mathcal{C})_{ij} \right.$$

$$\left. + \bar{T}^2 \sum_{i,j:\chi_i=+1} n_i (\mathcal{B}\mathcal{D}^{-1})_{ij} - \bar{T}^2 \sum_{i:\chi_i=-1} n_i \right), \tag{C8}$$

where in the second line we used Eq. (C7). For the bottom edge, we have reversed boundary conditions $\vec{\theta}_{ds}(0) = \bar{T}^2 \times (1, \ldots, 1)_k^T$ and $\vec{\theta}_{us}(L) = (\bar{T} + \Delta T)^2 \times (1, \ldots, 1)_{N-k}^T$. The bottom edge heat current (21) then reads

$$J_Q^{bot} = -\frac{\kappa_0}{2} \left(\sum_{i:\chi_i=+1} n_i \theta_{ds}^i(L) - \bar{T}^2 \sum_{i:\chi_i=-1} n_i \right)$$

$$= \frac{\kappa_0}{2} \left(\bar{T}^2 \sum_{i,j:\chi_i=+1} n_i (\mathcal{A} - \mathcal{B}\mathcal{D}^{-1}\mathcal{C})_{ij}(\bar{T} + \Delta T)^2 \right.$$

$$\left. + \sum_{i,j:\chi_i=+1} n_i (\mathcal{B}\mathcal{D}^{-1})_{ij} - (\bar{T} + \Delta T)^2 \sum_{i:\chi_i=-1} n_i \right). \tag{C9}$$

The crucial next step is the assumption that *the degrees of thermal equilibration on the top and bottom edges are identical.* This translates to identical block matrices $\mathcal{A}$, $\mathcal{B}$, $\mathcal{C}$, and $\mathcal{D}$ for the two edges. Then, and only then, can we combine the two currents as

$$J_Q^{top} - J_Q^{bot}$$

$$= \frac{\kappa_0}{2} ((\bar{T} + \Delta T)^2 + \bar{T}^2)$$

$$\times \left(\sum_{i,j:\chi_i=+1} n_i (\mathcal{A} - \mathcal{B}\mathcal{D}^{-1}\mathcal{C} + \mathcal{B}\mathcal{D}^{-1})_{ij} - \sum_{i:\chi_i=-1} n_i \right). \tag{C10}$$

Now, by using Eqs. (C5) and (C6), and identifying

$$\sum_{i:\chi_i=+1} n_i = c, \tag{C11}$$

$$\sum_{i:\chi_i=-1} n_i = \bar{c}, \tag{C12}$$

the dependence on $\mathcal{A}$, $\mathcal{B}$, $\mathcal{C}$, and $\mathcal{D}$ cancels out, and we find that Eq. (C10) reduces to

$$J_Q^{top} - J_Q^{bot} = \frac{\kappa_0}{2} ((\bar{T} + \Delta T)^2 + \bar{T}^2)(c - \bar{c}). \tag{C13}$$

Finally, inserting this expression into the definition of G_H^Q, given in Eq. (26), gives our desired result (27). Our proof generalizes the theoretical analysis for $\nu = 2/3$ in Ref. [37] to any edge structure.

APPENDIX D: COMPUTATION OF VOLTAGE AND TEMPERATURE PROFILES FOR THE phPf-3 INTERFACE

We compute the noise and thermal conductance of all considered edge structure by using voltage and temperature profiles of the edge channels within the incoherent tunneling model introduced in Sec. II. Below, we present in detail their derivation for the phPf-3 interface using boundary conditions for charge current as well as down- and upstream delta-T noise. Other edge structures are treated in a perfectly analogous manner.

We begin by labeling the edge channels as 1,2,3 from top to bottom according to Fig. 2. Transport along the edge is characterized by the channel specific filling factors ν_i, heat conductances n_i and chiralities χ_i, given by

(1) $\nu_1 = 1$, $n_1 = 1$, $\chi_1 = +$,
(2) $\nu_2 = 1/2$, $n_2 = 1$, $\chi_2 = -$,
(3) $\nu_3 = 0$, $n_3 = 1/2$, $\chi_3 = +$.

These values further specify the transport matrices $\mathcal{M}_V$ and $\mathcal{M}_T$ in Eqs. (4) and (7) as

$$
\mathcal{M}_T = \alpha \begin{pmatrix} -\chi_1 n_2 & \chi_1 n_2 & 0 \\ \chi_2 n_1 & -\chi_2 n_1 & 0 \\ 0 & 0 & 0 \end{pmatrix}
$$
$$
+ \beta \begin{pmatrix} 0 & 0 & 0 \\ 0 & -\chi_2 n_3 & \chi_2 n_3 \\ 0 & \chi_3 n_2 & -\chi_3 n_2 \end{pmatrix} \qquad \text{(D1)}
$$

and

$$
\mathcal{M}_V = \frac{1}{\ell_{\text{eq}}^C} \begin{pmatrix} -\frac{\chi_1}{\nu_1} & \frac{\chi_1}{\nu_1} \\ \frac{\chi_2}{\nu_2} & -\frac{\chi_2}{\nu_2} \end{pmatrix}. \qquad \text{(D2)}
$$

1. Charge current noise, $\Delta V \neq 0$, $\Delta T = 0$

For the charge current noise, the appropriate boundary conditions are

$$
T_i(0) = 0, \qquad \text{for} \quad i \in \{1, 2, 3\} \qquad \text{(D3a)}
$$

$$
V_i(0) = \Delta V, \quad \text{for} \quad \chi_i = +1 \qquad \text{(D3b)}
$$

$$
V_i(1) = 0, \qquad \text{for} \quad \chi_i = -1. \qquad \text{(D3c)}
$$

Here, we assumed that $e\Delta V \gg k_B \bar{T}$ so that we may set the base temperature $\bar{T} \to 0$. The voltage profiles $\vec{V}(\tilde{x})$ for the two charge carrying channels along the edge segment are obtained by solving Eq. (3). They are visualized in Fig. 13. Clearly the voltage drop occurs only on the right-hand side of the edge segment. This is the hot spot. Note also that the voltage profiles are independent of the degree of thermal equilibration, since the processes leading to charge and thermal equilibration are considered to take place at different lengthscales. Knowledge of $\vec{V}(\tilde{x})$ allows us to further compute the Joule heating contribution in Eq. (8). For efficient thermal equilibration, we next solve Eq. (6) and obtain temperature profiles, which depend on the pairwise degrees of thermal equilibration: $\alpha = L/\ell_{\text{eq},12}^Q$, $\beta = L/\ell_{\text{eq},23}^Q$ [see Eq. (24)], as well as the charge equilibration parameter $\delta = L/\ell_{\text{eq}}^C$. Here, L denotes the edge segment length and we define here $\tilde{x} = x/L$ as a rescaled coordinate along the segment. The channel resolved temperature profiles are visualized in Fig. 14(a) for two different sets of thermal equilibration lengths. We see that large α, β (red curves) are needed to have all channels at
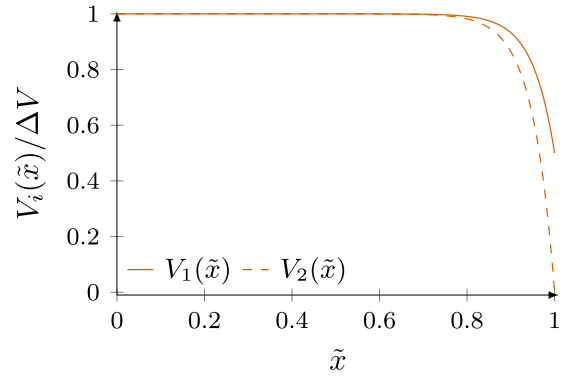

FIG. 13. Channel resolved voltage profiles $V_1(x)$ and $V_2(x)$ of the charge carrying channels at phPf-3 using $\delta = 20$.

similar temperatures at the noise spot (i.e., for $\tilde{x} \ll 1$) and thus to describe efficient thermal equilibration. This is contrasted by the blue curves for which α is not large and the channels are at different temperatures at the noise spot. Absent thermal equilibration on the other hand corresponds to $\ell_{\text{eq},ij}^Q \to \infty$ and Eq. (6) simplifies to

$$
\partial_{\tilde{x}} \vec{T}^2(\tilde{x}) = \delta \vec{V}(\tilde{x}). \qquad \text{(D4)}
$$

The channel resolved temperature profiles for this solution are given in Fig. 14(b).

2. Downstream delta-T noise, $\Delta V = 0$, $\Delta T \neq 0$

This type of noise corresponds to the boundary conditions

$$
V_i(0) = 0 = V_i(1), \quad \text{for} \quad i \in \{1, 2, 3\} \qquad \text{(D5a)}
$$

$$
T_i(0) = \bar{T} + \Delta T, \quad \text{for} \quad \chi_i = + \qquad \text{(D5b)}
$$

$$
T_i(1) = \bar{T}, \qquad \text{for} \quad \chi_i = - \qquad \text{(D5c)}
$$

which leads to trivial voltage profiles $V_i(\tilde{x}) \equiv 0$, $\forall i$. As a consequence, the energy transport equation Eq. (6) simplifies to

$$
\partial_{\tilde{x}} \vec{T}^2(\tilde{x}) = \mathcal{M}_T \vec{T}^2(\tilde{x}). \qquad \text{(D6)}
$$

For efficient thermal equilibration, this equation is solved to obtain temperature profiles in terms of (α, β). Here, we consider the strong temperature bias limit, $\Delta T \gg \bar{T}$, and consider the temperature profiles to leading order in $\Delta T/\bar{T}$. The resulting temperature profiles are shown in Fig. 14(c). In case of absent thermal equilibration, the energy transport equation reads

$$
\partial_{\tilde{x}} \vec{T}^2(\tilde{x}) = 0. \qquad \text{(D7)}
$$

Hence, the temperature profiles of the channels will be constant and follow immediately from the boundary conditions, see Fig. 14(d).

3. Upstream delta-T noise, $\Delta V = 0$, $\Delta T \neq 0$

For the upstream delta-T noise, we use the boundary conditions

$$
V_i(0) = 0 = V_i(1), \quad \text{for} \quad i \in \{1, 2, 3\} \qquad \text{(D8a)}
$$

$$
T_i(0) = \bar{T}, \qquad \text{for} \quad \chi_i = + \qquad \text{(D8b)}
$$

$$
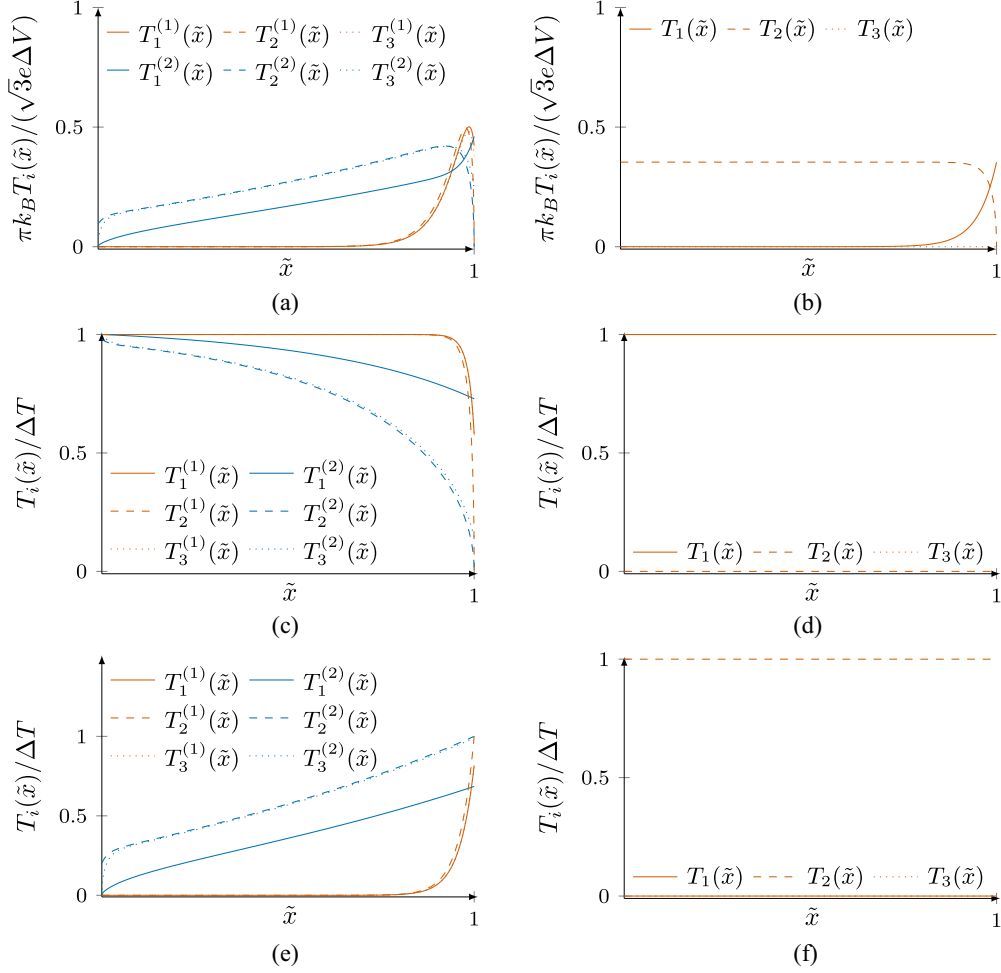T_i(1) = \bar{T} + \Delta T, \quad \text{for} \quad \chi_i = -. \qquad \text{(D8c)}
$$

FIG. 14. Channel resolved temperature profiles for channels 1, 2, and 3 of the phPf-3 interface. The distance along the edge segment is parametrized $\tilde{x} = x/L$. (a) Temperature profiles for voltage biased charge current noise for two sets of parameters: Superscript $^{(1)}$ labels profiles for the choice $(\alpha, \beta, \delta) = (100, 100, 20)$ (red lines) and $^{(2)}$ are profiles for $(\alpha, \beta, \delta) = (2, 100, 20)$ (blue lines). Both parameters sets correspond to finite thermal equilibration. (b) Same as (a) but for poor thermal equilibration. [(c),(d)] Same as (a) and (b) but for downstream delta-T noise for strong temperature bias $\Delta T \gg \bar{T}$. [(e),(f)] Same as (a) and (b) but for upstream delta-T noise for strong temperature bias $\Delta T \gg \bar{T}$.

Hence, the voltage profiles are also trivial $V_i(\tilde{x}) \equiv 0, \forall i$ and we obtain the temperature profiles using Eq. (D6) for efficient and Eq. (D7) for absent thermal equilibration. The resulting temperature profiles are visualized in Fig. 14(e) and Fig. 14(f), respectively.

4. Connection of temperature profiles to noise

The phPf-3 interface has $\nu_Q > 0$ so that for full thermal equilibration, the heat transport is dominantly in the downstream direction [see Fig. 2]. Any upstream heat transport is exponentially suppressed in L [66]. For the situation of voltage biased charge current noise, in the regime of efficient thermal equilibration, we find nonvanishing temperatures only in the region $\tilde{x} \approx 1$. This is seen from the red curves in Fig. 14(a). This characteristic region, called the *hot spot*, is a result of Joule heating close to the right (most downstream) contact and the dominantly downstream thermal transport. We

see that the effective temperature at the *noise spot* is very small: $T_{\text{ns}} \approx 0$, and we expect small noise as well $S \simeq 0$. Indeed, by inserting the temperature profiles in the noise kernel $\Lambda(x) = k_{\text{B}}T(\tilde{x})$ in Eq. (14) and integrating, we obtain exponentially suppressed noise $S \sim \exp(-\delta)$, plotted in Fig. 7(a).

For thermally equilibrated down- and upstream delta-T noise, the boundary conditions for an edge with $\nu_Q > 0$ imply equal and constant temperatures of all channels at the noise spot [see Figs. 14(c) and 14(e)]. This leads to a hot spot temperature $T_{\text{ns}} = \bar{T} + \Delta T$ and $T_{\text{ns}} = \bar{T}$ for down- and upstream delta-T noise respectively. The corresponding noise profiles are shown in Fig. 14(c). Absent thermal equilibration on the other hand leads to constant but different temperatures of the channels at the noise spot for the three cases. We explore the out-of-equilibrium situation in the noise spot by using the Green's function method outlined in Appendix B 1 to compute noise kernels $\Lambda(\tilde{x})$ with the full temperature

profiles in case of charge current noise. This leads to the noise plots in Fig. 7(b). For thermally nonequilibrated down- and upstream delta-T noise there is no additional source of heating along the edge. Following the same approach as for charge current noise in Appendix B 1, we find a modified NJ noise for down- and upstream delta-T noise, described by Eq. (38) and Eq. (41) respectively. Adjusting $\mathcal{M}_V$, $\mathcal{M}_T$ as well as the boundary conditions according to the transport properties of the involved channels, the temperature and noise profiles of the other interfaces in Fig. 7 are obtained following the same steps.

APPENDIX E: UNIT CONVERSION WITHOUT TEARS: FROM THEORIST TO EXPERIMENTALIST UNITS

The voltage bias noise excess noise S^{exc} computed using our approach is expressed in units of $e^3 \Delta V / h$. Let us denote the noise in such units as $S^{\mathrm{exc}}_{\Delta V}$. To connect these units to more experimentally relevant units, we start by using the current-voltage relation for chiral edge transport

$$I_0 = \nu \frac{e^2}{h} \Delta V. \tag{E1}$$

This relation holds for efficient charge equilibration, and is manifest experimentally by robust charge conductance quantization. By using this relation, we rewrite the noise in terms of the source current I_0 with the notation

$$S^{\mathrm{exc}}_{I_0} = \frac{S^{\mathrm{exc}}_{\Delta V}}{\Delta V} \frac{I_0}{\nu} \frac{h}{e^2}. \tag{E2}$$

For a voltage bias ΔV given in μV, the excess noise can then be written as

$$S^{\mathrm{exc}} \approx 6.20492 \left(\frac{S^{\mathrm{exc}}_{\Delta V}}{\Delta V e^3 / h} \right) \times 10^{-30} \frac{A^2}{\mu V \, \mathrm{Hz}}. \tag{E3}$$

Alternatively, for a bias current I_0 given in nA, we have

$$S^{\mathrm{exc}} \approx 1.602 \left(\frac{S^{\mathrm{exc}}_{\Delta V}}{\Delta V} \cdot \frac{I_0}{\nu} \right) \times 10^{-28} \frac{A^2}{\mathrm{nA \, Hz}}. \tag{E4}$$

[1] A. Stern, Non-Abelian states of matter, Nature (London) **464**, 187 (2010).

[2] A. Yu. Kitaev, Fault-tolerant quantum computation by anyons, Ann. Phys. **303**, 2 (2003).

[3] C. Nayak, S. H. Simon, A. Stern, M. Freedman, and S. Das Sarma, Non-Abelian anyons and topological quantum computation, Rev. Mod. Phys. **80**, 1083 (2008).

[4] D. C. Tsui, H. L. Stormer, and A. C. Gossard, Two-Dimensional Magnetotransport in the Extreme Quantum Limit, Phys. Rev. Lett. **48**, 1559 (1982).

[5] R. B. Laughlin, Anomalous Quantum Hall Effect: An Incompressible Quantum Fluid with Fractionally Charged Excitations, Phys. Rev. Lett. **50**, 1395 (1983).

[6] R. Willett, J. P. Eisenstein, H. L. Störmer, D. C. Tsui, A. C. Gossard, and J. H. English, Observation of an Even-Denominator Quantum Number in the Fractional Quantum Hall Effect, Phys. Rev. Lett. **59**, 1776 (1987).

[7] G. Moore and N. Read, Nonabelions in the fractional quantum Hall effect, Nucl. Phys. B **360**, 362 (1991).

[8] X. G. Wen, Non-Abelian Statistics in the Fractional Quantum Hall States, Phys. Rev. Lett. **66**, 802 (1991).

[9] N. Read and D. Green, Paired states of fermions in two dimensions with breaking of parity and time-reversal symmetries and the fractional quantum Hall effect, Phys. Rev. B **61**, 10267 (2000).

[10] K. K. W. Ma, M. R. Peterson, V. W. Scarola, and K. Yang, Fractional quantum Hall effect at the filling factor $\nu = 5/2$, arXiv:2208.07908 [cond-mat.mes-hall].

[11] B. Dutta, V. Umansky, M. Banerjee, and M. Heiblum, Isolated ballistic non-Abelian interface channel, Science **377**, 1198 (2022).

[12] B. Dutta, W. Yang, R. Melcer, H. K. Kundu, M. Heiblum, V. Umansky, Y. Oreg, A. Stern, and D. Mross, Distinguishing between non-Abelian topological orders in a quantum Hall system, Science **375**, 193 (2022).

[13] M. Levin, B. I. Halperin, and B. Rosenow, Particle-Hole Symmetry and the Pfaffian State, Phys. Rev. Lett. **99**, 236806 (2007).

[14] S.-S. Lee, S. Ryu, C. Nayak, and M. P. A. Fisher, Particle-Hole Symmetry and the $\nu = \frac{5}{2}$ Quantum Hall State, Phys. Rev. Lett. **99**, 236807 (2007).

[15] L. Fidkowski, X. Chen, and A. Vishwanath, Non-Abelian Topological Order on the Surface of a 3D Topological Superconductor from an Exactly Solved Model, Phys. Rev. X **3**, 041016 (2013).

[16] D. T. Son, Is the Composite Fermion a Dirac Particle? Phys. Rev. X **5**, 031027 (2015).

[17] P. T. Zucker and D. E. Feldman, Stabilization of the Particle-Hole Pfaffian Order by Landau-Level Mixing and Impurities That Break Particle-Hole Symmetry, Phys. Rev. Lett. **117**, 096802 (2016).

[18] L. Antonić, J. Vučičević, and M. V. Milovanović, Paired states at 5/2: Particle-hole Pfaffian and particle-hole symmetry breaking, Phys. Rev. B **98**, 115107 (2018).

[19] R. H. Morf, Transition from Quantum Hall to Compressible States in the Second Landau Level: New Light on the $\nu = 5/2$ Enigma, Phys. Rev. Lett. **80**, 1505 (1998).

[20] M. Storni, R. H. Morf, and S. Das Sarma, Fractional Quantum Hall State at $\nu = 5/2$ and the Moore-Read Pfaffian, Phys. Rev. Lett. **104**, 076803 (2010).

[21] A. Wójs, C. Tőke, and J. K. Jain, Landau-Level Mixing and the Emergence of Pfaffian Excitations for the 5/2 Fractional Quantum Hall Effect, Phys. Rev. Lett. **105**, 096802 (2010).

[22] E. H. Rezayi and S. H. Simon, Breaking of Particle-Hole Symmetry by Landau Level Mixing in the $\nu = 5/2$ Quantized Hall State, Phys. Rev. Lett. **106**, 116801 (2011).

[23] M. P. Zaletel, R. S. K. Mong, F. Pollmann, and E. H. Rezayi, Infinite density matrix renormalization group for multicomponent quantum Hall systems, Phys. Rev. B **91**, 045115 (2015).

[24] E. H. Rezayi, Landau Level Mixing and the Ground State of the $\nu = 5/2$ Quantum Hall Effect, Phys. Rev. Lett. **119**, 026801 (2017).

[25] S. H. Simon, M. Ippoliti, M. P. Zaletel, and E. H. Rezayi, Energetics of Pfaffian–anti-Pfaffian domains, Phys. Rev. B **101**, 041302 (2020).

[26] I. P. Radu, J. B. Miller, C. M. Marcus, M. A. Kastner, L. N. Pfeiffer, and K. W. West, Quasi-particle properties from tunneling in the v = 5/2 fractional quantum Hall state, Science **320**, 899 (2008).

[27] X. Lin, C. Dillard, M. A. Kastner, L. N. Pfeiffer, and K. W. West, Measurements of quasiparticle tunneling in the $\nu = \frac{5}{2}$ fractional quantum Hall state, Phys. Rev. B **85**, 165321 (2012).

[28] X. Lin, R. Du, and X. Xie, Recent experimental progress of fractional quantum Hall effect: 5/2 filling state and graphene, Natl. Sci. Rev. **1**, 564 (2014).

[29] X. G. Wen, Topological orders in rigid states, Int. J. Mod. Phys. B **04**, 239 (1990).

[30] P. Francesco, P. Mathieu, and D. Sénéchal, *Conformal Field Theory* (Springer Science & Business Media, New York, 2012).

[31] C. L. Kane and M. P. A. Fisher, Quantized thermal transport in the fractional quantum Hall effect, Phys. Rev. B **55**, 15832 (1997).

[32] A. Cappelli, M. Huerta, and G. R. Zemba, Thermal transport in chiral conformal theories and hierarchical quantum Hall states, Nucl. Phys. B **636**, 568 (2002).

[33] S. Jezouin, F. D. Parmentier, A. Anthore, U. Gennser, A. Cavanna, Y. Jin, and F. Pierre, Quantum limit of heat flow across a single electronic channel, Science **342**, 601 (2013).

[34] M. Banerjee, M. Heiblum, A. Rosenblatt, Y. Oreg, D. E. Feldman, A. Stern, and V. Umansky, Observed quantization of anyonic heat flow, Nature (London) **545**, 75 (2017).

[35] M. Banerjee, M. Heiblum, V. Umansky, D. E. Feldman, Y. Oreg, and A. Stern, Observation of half-integer thermal Hall conductance, Nature (London) **559**, 205 (2018).

[36] R. A. Melcer, B. Dutta, C. Spånslätt, J. Park, A. D. Mirlin, and V. Umansky, Absent thermal equilibration on fractional quantum Hall edges over macroscopic scale, Nat. Commun. **13**, 376 (2022).

[37] R. A. Melcer, S. Konyzheva, M. Heiblum, and V. Umansky, Direct determination of the topological thermal conductance via local power measurement, Nat. Phys. **19**, 327 (2023).

[38] S. K. Srivastav, M. R. Sahu, K. Watanabe, T. Taniguchi, S. Banerjee, and A. Das, Universal quantized thermal conductance in graphene, Sci. Adv. **5**, eaaw5798 (2019).

[39] S. K. Srivastav, R. Kumar, C. Spånslätt, K. Watanabe, T. Taniguchi, A. D. Mirlin, Y. Gefen, and A. Das, Vanishing Thermal Equilibration for Hole-Conjugate Fractional Quantum Hall States in Graphene, Phys. Rev. Lett. **126**, 216803 (2021).

[40] G. Le Breton, R. Delagrange, Y. Hong, M. Garg, K. Watanabe, T. Taniguchi, R. Ribeiro-Palau, P. Roulleau, P. Roche, and F. D. Parmentier, Heat Equilibration of Integer and Fractional Quantum Hall Edge Modes in Graphene, Phys. Rev. Lett. **129**, 116803 (2022).

[41] S. K. Srivastav, R. Kumar, C. Spånslätt, K. Watanabe, T. Taniguchi, A. D. Mirlin, Y. Gefen, and A. Das, Determination of topological edge quantum numbers of fractional quantum Hall phases by thermal conductance measurements, Nat. Commun. **13**, 5185 (2022).

[42] C. L. Kane and M. P. A. Fisher, Contacts and edge-state equilibration in the fractional quantum Hall effect, Phys. Rev. B **52**, 17393 (1995).

[43] I. Protopopov, Y. Gefen, and A. Mirlin, Transport in a disordered $\nu = 2/3$ fractional quantum Hall junction, Ann. Phys. **385**, 287 (2017).

[44] C. Nosiglia, J. Park, B. Rosenow, and Y. Gefen, Incoherent transport on the $\nu = 2/3$ quantum Hall edge, Phys. Rev. B **98**, 115408 (2018).

[45] A. Aharon-Steinberg, Y. Oreg, and A. Stern, Phenomenological theory of heat transport in the fractional quantum Hall effect, Phys. Rev. B **99**, 041302(R) (2019).

[46] K. K. W. Ma and D. E. Feldman, Thermal Equilibration on the Edges of Topological Liquids, Phys. Rev. Lett. **125**, 016801 (2020).

[47] F. Lafont, A. Rosenblatt, M. Heiblum, and V. Umansky, Counter-propagating charge transport in the quantum Hall effect regime, Science **363**, 54 (2019).

[48] Y. Cohen, Y. Ronen, W. Yang, D. Banitt, J. Park, M. Heiblum, A. D. Mirlin, Y. Gefen, and V. Umansky, Synthesizing a $\nu = 2/3$ fractional quantum Hall effect edge state from counter-propagating $\nu = 1$ and $\nu = 1/3$ states, Nat. Commun. **10**, 1920 (2019).

[49] S. H. Simon, Interpretation of thermal conductance of the $\nu = 5/2$ edge, Phys. Rev. B **97**, 121406 (2018).

[50] D. E. Feldman, Comment on "Interpretation of thermal conductance of the $\nu = 5/2$ edge", Phys. Rev. B **98**, 167401 (2018).

[51] H. Asasi and M. Mulligan, Partial equilibration of anti-Pfaffian edge modes at $\nu = 5/2$, Phys. Rev. B **102**, 205104 (2020).

[52] S. H. Simon and B. Rosenow, Partial Equilibration of the Anti-Pfaffian Edge due to Majorana Disorder, Phys. Rev. Lett. **124**, 126801 (2020).

[53] J. Park, C. Spånslätt, Y. Gefen, and A. D. Mirlin, Noise on the non-Abelian $\nu = 5/2$ Fractional Quantum Hall Edge, Phys. Rev. Lett. **125**, 157702 (2020).

[54] D. F. Mross, Y. Oreg, A. Stern, G. Margalit, and M. Heiblum, Theory of Disorder-Induced Half-Integer Thermal Hall Conductance, Phys. Rev. Lett. **121**, 026801 (2018).

[55] C. Wang, A. Vishwanath, and B. I. Halperin, Topological order from disorder and the quantized Hall thermal metal: Possible applications to the $\nu = 5/2$ state, Phys. Rev. B **98**, 045112 (2018).

[56] B. Lian and J. Wang, Theory of the disordered $\nu = \frac{5}{2}$ quantum thermal Hall state: Emergent symmetry and phase diagram, Phys. Rev. B **97**, 165124 (2018).

[57] W. Zhu, D. N. Sheng, and K. Yang, Topological Interface between Pfaffian and Anti-Pfaffian Order in $\nu = 5/2$ Quantum Hall Effect, Phys. Rev. Lett. **125**, 146802 (2020).

[58] P.-S. Hsin, Y.-H. Lin, N. M. Paquette, and J. Wang, Effective field theory for fractional quantum Hall systems near $\nu = 5/2$, Phys. Rev. Res. **2**, 043242 (2020).

[59] I. C. Fulga, Y. Oreg, A. D. Mirlin, A. Stern, and D. F. Mross, Temperature Enhancement of Thermal Hall Conductance Quantization, Phys. Rev. Lett. **125**, 236802 (2020).

[60] S. Das, S. Das, and S. S. Mandal, An anomalous reentrant 5/2 quantum Hall phase at moderate Landau-Level-mixing strength, arXiv:2206.04419.

[61] T. Giamarchi and H. J. Schulz, Anderson localization and interactions in one-dimensional metals, Phys. Rev. B **37**, 325 (1988).

[62] I. V. Gornyi, A. D. Mirlin, and D. G. Polyakov, Electron transport in a disordered Luttinger liquid, Phys. Rev. B **75**, 085421 (2007).

[63] C. Spånslätt, A. Stern, and A. D. Mirlin, Transport signatures of fractional quantum Hall binding transitions, arXiv:2302.05781 [Phys. Rev. B (to be published)].

[64] M. Yutushui, A. Stern, and D. F. Mross, Identifying the $\nu = \frac{5}{2}$ Topological Order through Charge Transport Measurements, Phys. Rev. Lett. **128**, 016401 (2022).

[65] J. Park, A. D. Mirlin, B. Rosenow, and Y. Gefen, Noise on complex quantum Hall edges: Chiral anomaly and heat diffusion, Phys. Rev. B **99**, 161302 (2019).

[66] C. Spånslätt, J. Park, Y. Gefen, and A. D. Mirlin, Topological Classification of Shot Noise on Fractional Quantum Hall Edges, Phys. Rev. Lett. **123**, 137701 (2019).

[67] C. Spånslätt, J. Park, Y. Gefen, and A. D. Mirlin, Conductance plateaus and shot noise in fractional quantum Hall point contacts, Phys. Rev. B **101**, 075308 (2020).

[68] Note that when interfacing the $\nu = 5/2$ edge with $n = 3$, the downstream and upstream directions are swapped. The sign of ν_Q is then adjusted so that $\nu_Q > 0$ corresponds to the direction of the equilibrated charge flow.

[69] X. Wan, K. Yang, and E. H. Rezayi, Edge Excitations and Non-Abelian Statistics in the Moore-Read State: A Numerical Study in the Presence of Coulomb Interaction and Edge Confinement, Phys. Rev. Lett. **97**, 256804 (2006).

[70] X. Wan, Z.-X. Hu, E. H. Rezayi, and K. Yang, Fractional quantum Hall effect at $\nu = 5/2$: Ground states, non-Abelian quasiholes, and edge modes in a microscopic model, Phys. Rev. B **77**, 165316 (2008).

[71] B. Overbosch and X.-G. Wen, Phase transitions on the edge of the $\nu = 5/2$ Pfaffian and anti-Pfaffian quantum Hall state, arXiv:0804.2087 (2008).

[72] Y. Zhang, Y.-H. Wu, J. A. Hutasoit, and J. K. Jain, Theoretical investigation of edge reconstruction in the $\nu = 5/2$ and 7/3 fractional quantum Hall states, Phys. Rev. B **90**, 165104 (2014).

[73] S. Manna, A. Das, M. Goldstein, and Y. Gefen, Full classification of transport on an equilibrated 5/2 edge, arXiv:2212.05732.

[74] T. Fujisawa, Nonequilibrium charge dynamics of Tomonaga–Luttinger liquids in quantum Hall edge channels, Ann. Phys. (Leipzig) **534**, 2100354 (2022).

[75] R. Kumar, S. K. Srivastav, C. Spånslätt, K. Watanabe, T. Taniguchi, Y. Gefen, A. D. Mirlin, and A. Das, Observation of ballistic upstream modes at fractional quantum Hall edges of graphene, Nat. Commun. **13**, 213 (2022).

[76] M. Hein, Impact of equilibration on the heat conductance and noise of non-abelian fractional quantum hall edges, Master's thesis, Chalmers University of Technology, 2022.

[77] C. Spånslätt, Y. Gefen, I. V. Gornyi, and D. G. Polyakov, Contacts, equilibration, and interactions in fractional quantum Hall edge transport, Phys. Rev. B **104**, 115416 (2021).

[78] H. Nyquist, Thermal agitation of electric charge in conductors, Phys. Rev. **32**, 110 (1928).

[79] J. B. Johnson, Thermal agitation of electricity in conductors, Phys. Rev. **32**, 97 (1928).

[80] O. S. Lumbroso, L. Simine, A. Nitzan, D. Segal, and O. Tal, Electronic noise due to temperature differences in atomic-scale junctions, Nature (London) **562**, 240 (2018).

[81] J. Rech, T. Jonckheere, B. Grémaud, and T. Martin, Negative Delta-T Noise in the Fractional Quantum Hall Effect, Phys. Rev. Lett. **125**, 086801 (2020).

[82] N. Schiller, Y. Oreg, and K. Snizhko, Extracting the scaling dimension of quantum Hall quasiparticles from current correlations, Phys. Rev. B **105**, 165150 (2022).

[83] G. Zhang, I. V. Gornyi, and C. Spånslätt, Delta-T noise for weak tunneling in one-dimensional systems: Interactions versus quantum statistics, Phys. Rev. B **105**, 195423 (2022).

[84] G. Rebora, J. Rech, D. Ferraro, T. Jonckheere, T. Martin, and M. Sassetti, Delta-T noise for fractional quantum Hall states at different filling factor, Phys. Rev. Res. **4**, 043191 (2022).

[85] C. L. Kane, M. P. A. Fisher, and J. Polchinski, Randomness at the Edge: Theory of Quantum Hall Transport at Filling $\nu = 2/3$, Phys. Rev. Lett. **72**, 4129 (1994).

[86] C. L. Kane and M. P. A. Fisher, Impurity scattering and transport of fractional quantum Hall edge states, Phys. Rev. B **51**, 13449 (1995).

[87] J. E. Moore and X.-G. Wen, Classification of disordered phases of quantum Hall edge states, Phys. Rev. B **57**, 10138 (1998).

[88] I. Safi and H. J. Schulz, Transport in an inhomogeneous interacting one-dimensional system, Phys. Rev. B **52**, R17040(R) (1995).

[89] I. V. Krive, Thermal transport through Luttinger liquid constriction, Low Temp. Phys. **24**, 377 (1998).

[90] D.-K. Ki, V. I. Fal'ko, D. A. Abanin, and A. F. Morpurgo, Observation of even denominator fractional quantum Hall effect in suspended bilayer graphene, Nano Lett. **14**, 2135 (2014).

[91] Y. Kim, D. S. Lee, S. Jung, V. Skákalová, T. Taniguchi, K. Watanabe, J. S. Kim, and J. H. Smet, Fractional quantum Hall states in bilayer graphene probed by transconductance fluctuations, Nano Lett. **15**, 7445 (2015).

[92] A. A. Zibrov, C. Kometter, H. Zhou, E. M. Spanton, T. Taniguchi, K. Watanabe, M. P. Zaletel, and A. F. Young, Tunable interacting composite fermion phases in a half-filled bilayer-graphene Landau level, Nature (London) **549**, 360 (2017).

[93] A. A. Zibrov, E. M. Spanton, H. Zhou, C. Kometter, T. Taniguchi, K. Watanabe, and A. F. Young, Even-denominator fractional quantum Hall states at an isospin transition in monolayer graphene, Nat. Phys. **14**, 930 (2018).

[94] J. I. A. Li, C. Tan, S. Chen, Y. Zeng, T. Taniguchi, K. Watanabe, J. Hone, and C. R. Dean, Even-denominator fractional quantum Hall states in bilayer graphene, Science **358**, 648 (2017).

[95] Y. Kim, A. C. Balram, T. Taniguchi, K. Watanabe, J. K. Jain, and J. H. Smet, Even denominator fractional quantum Hall states in higher Landau levels of graphene, Nat. Phys. **15**, 154 (2019).

[96] K. Huang, H. Fu, D. R. Hickey, N. Alem, X. Lin, K. Watanabe, T. Taniguchi, and J. Zhu, Valley Isospin Controlled Fractional Quantum Hall States in Bilayer Graphene, Phys. Rev. X **12**, 031019 (2022).

[97] N. Read and E. Rezayi, Beyond paired quantum Hall states: Parafermions and incompressible states in the first excited Landau level, Phys. Rev. B **59**, 8084 (1999).

[98] J. S. Xia, W. Pan, C. L. Vicente, E. D. Adams, N. S. Sullivan, H. L. Stormer, D. C. Tsui, L. N. Pfeiffer, K. W. Baldwin, and

K. W. West, Electron Correlation in the Second Landau Level: A Competition Between Many Nearly Degenerate Quantum Phases, Phys. Rev. Lett. **93**, 176809 (2004).

[99] A. Kumar, G. A. Csáthy, M. J. Manfra, L. N. Pfeiffer, and K. W. West, Nonconventional Odd-Denominator Fractional Quantum Hall States in the Second Landau Level, Phys. Rev. Lett. **105**, 246808 (2010).

[100] T. Martin, Noise in mesoscopic physics, in *Proceedings of the Les Houches Summer School, Session LXXXI*, edited by H. Bouchiat, Y. Gefen, S. Guéron, G. Montambaux, and J. Dalibard (Elsevier, New York, 2005).

[101] L. E. Turner, The Mittag-Leffler theorem: The origin, evolution, and reception of a mathematical result, 1876–1884, Historia Mathematica **40**, 36 (2013).